

Ultra-low loss piezo-optomechanical low-confinement silicon nitride platform for visible wavelength quantum photonic circuits

Mayank Mishra¹, Gwangho Choi¹, Wenhua He¹, Gina M. Talcott²,
Katherine Kearney², Michael Gehl², Andrew Leenheer²,
Daniel Dominguez², Nils T. Otterstrom^{2*}, Matt Eichenfield^{1,2,3*}

¹James C. Wyant College of Optical Sciences, University of Arizona,
Tucson, Arizona, 85721, USA.

²Microsystems Engineering, Science, and Applications, Sandia National
Laboratories, Albuquerque, New Mexico, 87185, USA.

³Electrical, Computer and Energy Engineering, University of Colorado,
Boulder, Colorado, 80309, USA.

*Corresponding author(s). E-mail(s): ntotter@sandia.gov;
Matt.Eichenfield@colorado.edu;

Abstract

The stringent demands of photonic quantum computing protocols motivate photonic integrated circuit (PIC) platforms with passive optical properties such as extremely low losses and correspondingly large circuit depths, as well as active optical properties such as high reconfiguration rates, low power dissipation, and minimal crosstalk. At the same time, many quantum photonic resource state generators, such as single-photon sources and quantum memories, require operation in the visible wavelength range. These requirements make the passive optical properties of CMOS-fabricated, ultralow-loss, low-confinement silicon nitride waveguides especially attractive. However, the conventional active properties of these systems based on thermo-optic modulation are plagued by high levels of crosstalk, slow modulation rates, and high power dissipation. Although there have been recent demonstrations of CMOS-fabricated, visible wavelength, piezo-optomechanical PICs that solve the above challenges associated with implementing active functionality, these have made use of high-confinement waveguides with currently demonstrated losses of order **0.3–1 dB/cm**, precluding circuit depths required for scalable quantum algorithms. Here, we demonstrate that combining piezo-optomechanical actuation with a low-confinement, ultra-low loss

silicon nitride platform addresses the scalability challenge while enabling high-performance active functionality at visible wavelengths. This platform achieves a propagation loss **0.026 dB/cm** at **780 nm**, modulation bandwidths in the MHz range, and a phase shifter voltage-length product ($V_\pi L$) of approximately **2.8 V · m** and negligible hysteresis. We further demonstrate reconfigurable Mach-Zehnder interferometers based on spiral phase shifters with 0.63 dB loss per phase shifter.

Introduction

Recent work in high-confinement, piezo-optomechanical photonic integrated circuits (PICs) in the visible wavelength regime has demonstrated high circuit densities, fast modulation rates, and low power dissipation/consumption [1–6]. Given this set of capabilities, piezo-optomechanical PICs could be well-suited for visible wavelength scalable quantum photonic information processing applications such as integrated quantum resource state generators [7], linear optical computing [8], hybrid spin-photon quantum computing architectures [6], quantum networking protocols [9], and quantum sensors [10]. However, the propagation losses in these high-confinement waveguides remain, in many cases, too high to achieve the circuit depths and low error rates necessary for scalable quantum computing [11]. In contrast, low-confinement silicon nitride (Si_3N_4) waveguides, which feature high-aspect ratio silicon nitride cores and extremely thick silicon dioxide claddings, have the potential to address this scaling challenge by offering ultra-low propagation losses [12, 13]. These waveguides have shown exceptionally low optical losses of less than 0.1 dB/m [14, 15] at telecommunication wavelengths and below 1 dB/m [16, 17] at visible wavelengths. These low-confinement waveguide platforms deliver high optical power-handling capabilities and a wide transparency window [18, 19]. Furthermore, they support the realization of ultra-high-Q resonators [20] and provide a pathway for integration with quantum systems, including rubidium atoms [21], strontium atoms [22], and InAs quantum dots [23].

The integration of thermo-optic modulators [20, 24, 25] and PZT-based piezo-optomechanical actuators [26–28] with low-confinement silicon nitride waveguides has been demonstrated, but both approaches exhibit significant limitations. Thermo-optic modulators typically exhibit slow modulation speeds, high power consumption/dissipation, and large crosstalk. On the other hand, PZT-based devices offer higher modulation speed and lower crosstalk but suffer from significant ferroelectric hysteresis and integration limitations due to CMOS-incompatibility. In contrast, piezo-optomechanical actuator platforms based on aluminum nitride (AlN) implemented using CMOS foundry processes offer a promising alternative [1–3, 5, 29]. Although so far only demonstrated with high-confinement waveguides, these AlN actuators provide high modulation bandwidths (exceeding 100 MHz), ultralow power consumption with negligible hysteresis, and compatibility with cryogenic operation.

The much thicker silicon dioxide claddings required by low-confinement silicon nitride waveguides present a key challenge for piezo-optomechanical actuation and strain-optic phase shifters. Without careful design, the increased oxide thickness leads

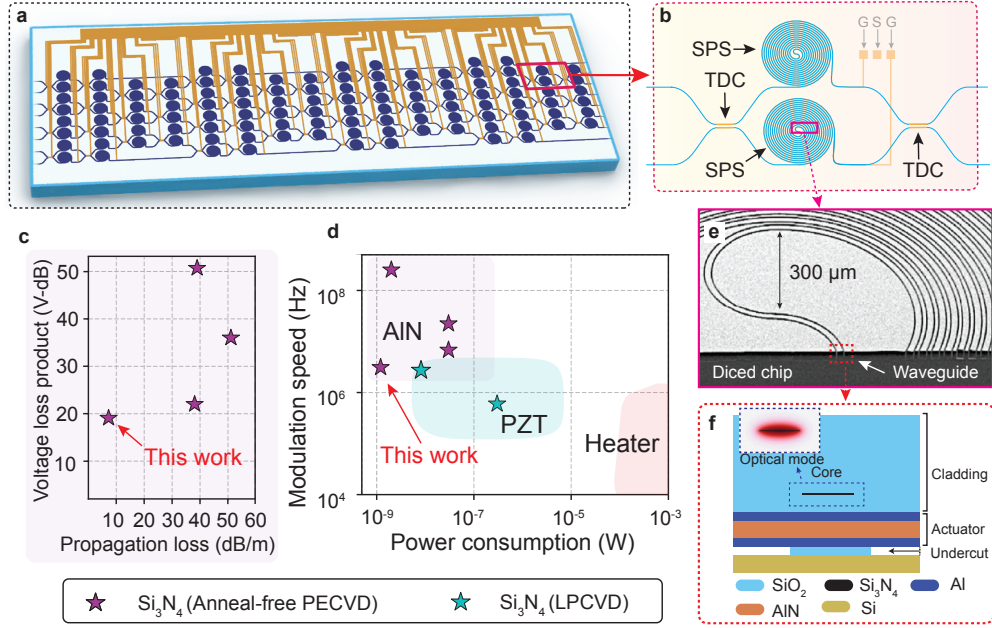


Fig. 1 Low-confinement silicon nitride piezo-optomechanical platform.

(a) Schematic representation of the eight-mode linear programmable nanophotonic processor (LPNP) circuit, based on the Clements et al. [30] architecture, featuring a network of Mach-Zehnder interferometers (MZIs) and phase shifters. (b) Schematic of an MZI incorporating two Archimedean spiral phase shifters (SPSs) and two tunable directional couplers (TDCs). (c) Comparison of the voltage-loss product (VLP) and propagation loss across existing visible wavelength aluminum nitride-based piezo-optomechanical modulator platforms [1, 2]. (d) Comparison of modulation speed and power consumption for visible wavelength silicon nitride (Si_3N_4) based modulator platforms [1, 2, 24, 26, 28]. The Si_3N_4 platforms include devices fabricated via low-pressure chemical vapor deposition (LPCVD) and anneal-free plasma-enhanced chemical vapor deposition (PECVD). Details on the loss and VLP values for existing visible wavelength Si_3N_4 platforms are provided in Supplementary Table 1. (e) Scanning electron microscope (SEM) image showing the cross-section of a wafer diced through the center of an on-chip SPS, with a minimum bending radius of $150\ \mu\text{m}$ at the center. (f) Cross-sectional schematic of a low-confinement waveguide-based piezo-optomechanical phase modulator, highlighting the different material layers. Inset: x-component of the electric field of the fundamental optical mode in a low-confinement waveguide, simulated using the finite element method.

to high mechanical rigidity and, consequently, reduced piezo-optomechanical responsivity. In this work, we show that thick silicon dioxide claddings with an extended undercut beneath the actuator can enable geometries and aspect ratios that concentrate the distribution of stress and optical field within the core and cladding of the waveguide in a way that allows high piezo-optomechanical responsivity even with thick claddings. Moreover, because a large fraction of the optical field in these low-confinement waveguides resides in the silicon dioxide cladding, the comparatively stronger photoelastic response of silicon dioxide [29, 31], despite its lower refractive index than silicon nitride, compensates for the reduced mechanical compliance (see Supplementary Fig. 3d and Supplementary Fig. 3e). Experimentally,

we demonstrate a design achieving piezo-optomechanical responsivity comparable to high-confinement systems while lowering optical loss by an order of magnitude [1]. In the following sections, we present the device performance and loss characterization of our low-confinement platform, and show, through an example, how reduced loss leads to orders-of-magnitude improvements in the success probability of heralding multi-photon quantum states in LPNP circuits.

Results

Low-confinement waveguide platform

The fundamental programmable element of low-confinement waveguide linear programmable nanophotonic processor (LPNP) platform (Fig. 1a) is a Mach-Zehnder interferometer (MZI; Fig. 1b) with integrated output phase shifters. These MZIs utilize Archimedean-spiral-shaped waveguide phase shifters to reduce both the device footprint and optical bending losses. A scanning electron micrograph of a spiral phase-shifter (SPS) section fabricated using an anneal-free plasma-enhanced chemical vapor deposition (PECVD) process [1, 2, 5, 32] is shown in Fig. 1e. Compared to conventional low-pressure chemical vapor deposition (LPCVD), the anneal-free PECVD approach enables low-temperature processing, allowing seamless monolithic integration with CMOS metal routing for the actuator beneath the waveguide, which would otherwise be damaged by high-temperature annealing. As detailed in subsequent sections and highlighted in Fig. 1c, our low-confinement waveguides establish a new benchmark in voltage-loss product (VLP) and propagation loss among visible wavelength, anneal-free PECVD-fabricated silicon nitride waveguides with AlN piezo-optomechanical actuators. Additionally, as shown in Fig. 1d, these devices achieve high modulation speeds in the MHz range and exhibit low holding power in the nanowatt range ($P_{\text{hold}} < 1$ nW for a 5 V applied voltage at room temperature), comparable to other visible wavelength modulators employing AlN-based piezo-optomechanical strain actuator platforms [1, 2].

Fig. 1f illustrates the integration of the low-confinement waveguide with a piezo-optomechanical actuator. A scanning electron micrograph of the waveguide is shown in Fig. 2a, with the thin core highlighted in yellow (false color). The fabricated waveguide features a 50 nm-thick, 3.6 μm -wide core, positioned 2.96 μm above the actuator, and is embedded within a SiO_2 cladding that is 12.5 μm -thick and 15.8 μm -wide at the core height, as depicted in Fig. 2a. The actuator, shown in Fig. 2b, consists of a 0.46 μm -thick aluminum nitride layer sandwiched between two 0.25 μm -thick aluminum electrodes, connected to electrical signals through ground-signal-ground (GSG) contact pads. To characterize the SPS, we integrate it into one arm of an imbalanced MZI, as illustrated in Fig. 2c. Adiabatic tapers (2 mm long) at both input and output ports gradually widen the core from 0.4 μm to 3.6 μm , ensuring fundamental mode excitation [33] and minimizing coupling loss.

When a voltage difference ΔV is applied across the electrical contacts, it generates a vertical electric field given by $E_3 \approx \Delta V/t_{\text{AlN}}$, where t_{AlN} is the AlN layer thickness. This electric field induces strain in the structure, described by the strain

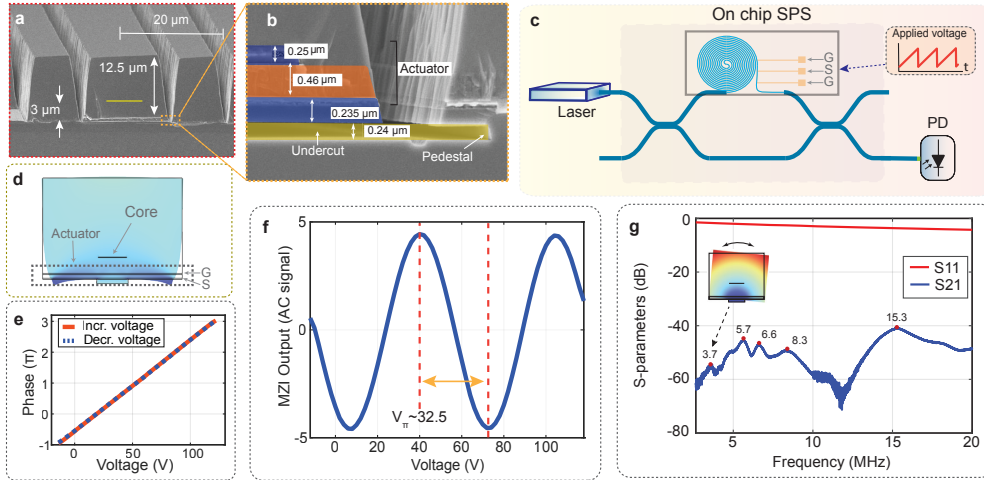


Fig. 2 Piezo-optomechanical phase shifter characterization.

(a, b) Cross-sectional SEM images of the fabricated phase modulators. In (b), blue and orange false colors highlight the electrode and the AlN actuator layer, respectively, which is suspended by an undercut. (c) Schematic of the imbalanced MZI used for characterization, incorporating an on-chip spiral phase shifter in one arm, two off-chip 50:50 beam splitters, a 780 nm laser, and a photodetector. A ramp voltage (red) is applied to the piezo-optomechanical actuator, modulating the phase and producing a sinusoidal optical output. (d) Schematic cross-section of the phase shifter with FEM-simulated s_{11} strain distribution and the corresponding (exaggerated) waveguide deformation for clarity. (e) Measured phase response of the MZI for increasing and decreasing voltage sweeps from -10 V to 120 V and back, showing negligible hysteresis. (f) Measured optical response of the MZI under a 200 Hz ramp voltage applied to the piezo-optomechanical SPS. An 8.7 cm SPS achieves a π phase shift at 32.5 V. (g) Measured S-parameter spectra (S11, S21) of the SPS, showing strong S21 resonances at 3.7, 5.7, 6.6, and 8.3 MHz and negligible S11 response over 0–20 MHz. Inset: simulated mechanical eigenmode at 3.7 MHz.

tensor s_{kl} , with the s_{11} component illustrated in Fig. 2d. The induced strain modulates the effective refractive index (n_{eff}) of the waveguide via two primary mechanisms: the photoelastic effect ($\Delta n_{\text{eff,PE}}$) and the moving boundary effect ($\Delta n_{\text{eff,MB}}$) [5, 29]. The relative change of refractive index under strain is conventionally described by the strain-optic coefficient as $\Delta(1/n^2)_{ij} = \sum_{k,l} p_{ijkl} s_{kl}$, where p_{ijkl} is the photoelastic tensor [29, 31, 34]. The strain components are related to the applied electric field by $s_{kl} = \sum_m d_{mkl} E_m$, where d_{mkl} represents the piezoelectric coupling tensor. The total change in effective refractive index per applied volt, $\Delta n_{\text{eff}} = \Delta n_{\text{eff,PE}} + \Delta n_{\text{eff,MB}}$, produces a phase shift in the optical mode given by $\Delta\phi = \frac{2\pi}{\lambda} \Delta n_{\text{eff}} L$. Using two-dimensional finite element method (FEM) simulations of the waveguide cross section (as shown in Fig. 2d and the inset of Fig. 1f), we calculate the voltage-length product ($V_{\pi}L$):

$$V_{\pi}L = \frac{\lambda}{2} \left(\frac{\Delta n_{\text{eff}}}{\Delta V} \right)^{-1}, \quad (1)$$

where $\Delta n_{\text{eff}}/\Delta V$ is the change in the effective refractive index per applied volt. Supplementary Fig. 6 and Fig. 7 further analyze how $V_{\pi}L$ varies with geometry.

To characterize the modulator, we apply a 200 Hz ramp signal to the SPS, sweeping the voltage from -10 V to 120 V. The resulting optical response exhibits sinusoidal fringes due to the MZI transfer function, with negligible hysteresis between the forward and reverse voltage sweeps, as shown in Fig. 2e. From these measurements, we extract an average V_π of approximately 32.5 V. For the 8.7-cm-long spiral phase shifter at $\lambda = 780$ nm, this corresponds to a voltage-length product of $V_\pi L = 2.8$ V \cdot m. Additional measurement details on other tested devices are provided in Supplementary Fig. 4.

These devices are tested well below any mechanical resonance frequencies. Although operating at or above resonance can enhance the optomechanical response, it also induces narrowband behavior, ringing, and phase lag, so the fundamental eigenfrequency ultimately sets the upper limit of the usable bandwidth. We characterized the mechanical resonance frequencies using a vector network analyzer (VNA), as shown in Fig. 2G. The transmission coefficient S_{21} exhibits prominent resonance peaks at 3.7 MHz (fundamental), 5.7 MHz, 6.6 MHz, and 8.3 MHz, while the reflection coefficient S_{11} shows negligible response over the 0–20 MHz range. From the observed fundamental eigenfrequency of 3.7 MHz, we estimate the pedestal width of our devices using FEM simulations to be approximately 1.4 μm . Using this geometry in the simulations, together with the experimentally measured $V_\pi L = 2.8$ V \cdot m and reported literature values for $|p_{12}|$ and $|p_{44}|$ [29], we evaluate the possible values of the silicon nitride photoelastic coefficients. Because $p_{44} = (p_{11} - p_{12})/2$, there are four candidate combinations of p_{11} and p_{12} , and only $p_{11} = -0.125$ and $p_{12} = 0.047$ yield simulated values of $V_\pi L$ consistent with the experimental measurement of 2.8 V \cdot m. These findings indicate that silicon dioxide dominates the strain-induced effective refractive index change, whereas silicon nitride contributes an opposing effect, as discussed in Supplementary Note 1 and Note 2.

Loss characterization of low-confinement waveguide

The overall attenuation (α) of optical modes in low-confinement waveguides arises from both intrinsic material properties and device geometry. Advances in fabrication have substantially reduced material absorption losses [35], making geometry-dependent losses the primary contributors to total attenuation. These losses include (i) actuator absorption, (ii) scattering from interfacial roughness, (iii) radiation from waveguide bends, (iv) mode coupling loss at the fiber-to-waveguide interface, and (v) crosstalk between adjacent waveguides. Among these, absorption and scattering losses are particularly sensitive to waveguide dimensions (see Supplementary Note 6 and Supplementary Fig. 7), as variations in core and cladding size can significantly alter modal overlap with absorptive or rough regions. We combine FEM simulations with analytical loss models to estimate the propagation loss in our low-confinement platform, as described in Supplementary Note 7 and illustrated in Supplementary Fig. 7 and Fig. 8. Using the estimated photoelastic constants, we identify an optimal waveguide geometry by minimizing the voltage-loss product, as discussed in Supplementary Note 6 and Note 8 and summarized in Supplementary Fig. 8.

We characterized the propagation loss using a top-down imaging technique (Ref. [36], Fig. 3a) in two distinct low-confinement waveguide geometries: (i) an unetched waveguide without an actuator (Fig. 3c) and (ii) an etched waveguide with

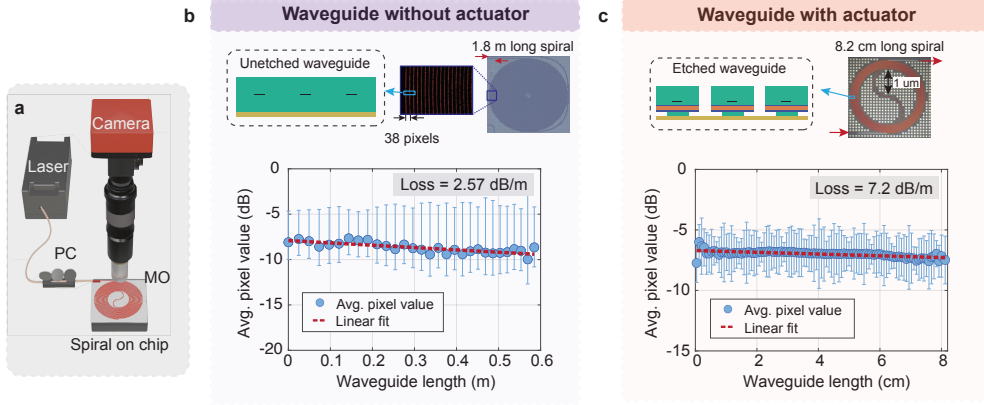


Fig. 3 Waveguide-loss measurement using top-view imaging.

(a) Schematic of the experimental setup for measuring waveguide loss using a top-down micrograph technique. The setup includes a 780 nm laser, polarization controller (PC), and a camera equipped with a $12\times$ zoom lens and a $5\times$ microscope objective (MO). (b) Propagation loss characterization of an unetched 1.8 m silicon nitride Archimedean spiral waveguide (no actuator). Image analysis of a spiral section shows the average pixel intensity versus propagation distance; linear fitting yields a loss of 2.57 dB/m. (c) Propagation loss analysis of an etched 8.2 cm-long Archimedean spiral waveguide with an integrated bottom actuator. Image processing of the complete spiral structure and pixel-intensity averaging along its length yield a propagation loss of 7.2 dB/m.

a bottom actuator (Fig. 3d). In the unetched device, the dominant loss mechanism is scattering at the core-cladding interface due to fabrication imperfections. By contrast, the etched waveguide with an integrated actuator exhibits additional losses from actuator absorption as well as scattering at both the core-cladding and cladding-air interfaces. The top-down imaging technique (Fig. 3a) collects light scattered perpendicular to the direction of optical mode propagation. This method is based on the principle that the local intensity of scattered light is directly proportional to the remaining guided power within the waveguide. For the unetched waveguide shown in Fig. 3c, we image a section of the 1.8-m-long Archimedean spiral, where adjacent waveguides in the image are separated by approximately 38 pixels, corresponding to 2.4 cm of waveguide length along the spiral. We apply a 20-pixel-wide analysis window following the waveguide curvature to calculate the average pixel intensity for each waveguide segment. By plotting these intensity values against the propagation length of the optical mode along the spiral and performing a linear fit, we extract a propagation loss of 2.57 dB/m.

For the etched waveguide with actuator shown in Fig. 3d, we image the entire 8.2-cm-long spiral in a single field of view and average pixel intensities along its length. We divide the spiral into 100 sections and each 0.82-mm-long section corresponds to a data point in the Fig. 3d plot. In each section, we apply a 15-pixel averaging window that covers the waveguide. Linear fitting of these data points yields a propagation loss of 7.2 dB/m, approximately 2.8 higher than in the unetched case. We cross-validate these results using optical time-domain reflectometry (OTDR) with a femtosecond laser, which yields a propagation loss of 6.1 dB/m for the actuator-free waveguide,

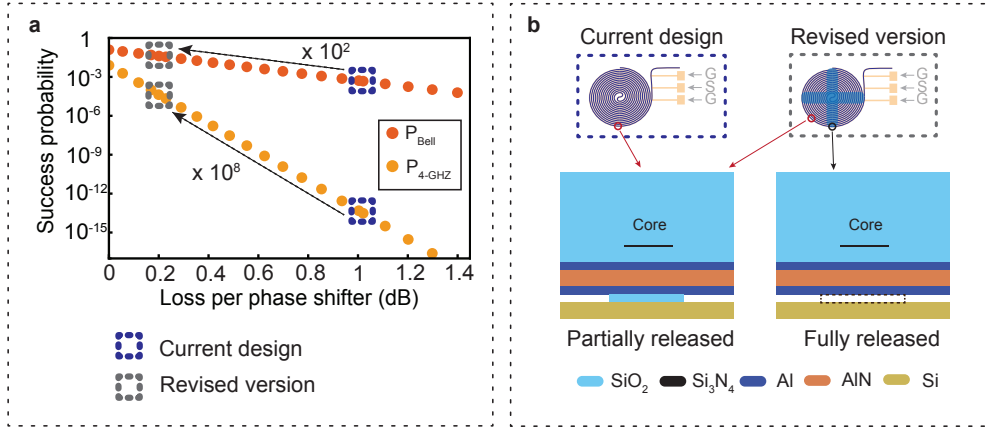


Fig. 4 Simulated performance scaling and proposed SPS geometry.

(a) Success probability for generating heralded Bell states and 4-mode GHZ states within a lossy LPNP circuit. The arrows highlight the significant improvement in success probability achieved by reducing the loss per phase shifter from 1 dB/m to 0.2 dB/m; this reduction yields probability enhancement factors of $\sim 10^2$ for Bell states and $\sim 10^8$ for 4-mode GHZ states (see Supplementary Note 4 for details). (b) Schematic of two SPS designs: the presently demonstrated device (partially released) and a proposed revised version (with fully released sections). The revised design aims to minimize the propagation loss per phase shifter in the LPNP circuit toward the low-loss regime (0.2 dB/m) simulated in (a).

while direct transmission measurements provide a propagation loss of 3.8 dB/m and an insertion loss of 1.9 dB per facet. These complementary techniques show reasonable agreement with the imaging-based results and confirm that propagation losses remain below 10 dB/m across all measurement methods. Detailed analysis procedures, noise correction methods, and measurement protocols are provided in Supplementary Note 5 and Supplementary Fig. 6.

Discussion

Using a top-down propagation loss measurement approach, we measure propagation losses of 7.2 dB/m with an actuator and 2.57 dB/m without an actuator for our low-confinement waveguides fabricated via the PECVD process. The higher loss in waveguides with actuators is attributed to additional modal absorption by the top metal electrodes. We employ these waveguides as phase shifters with a length of 8.7 cm and propagation loss of 0.626 dB, achieving a voltage-length product of approximately $2.8 \text{ V} \cdot \text{m}$ at 780 nm, corresponding to a VLP of about $20.16 \text{ V} \cdot \text{dB}$. In comparison, state-of-the-art high-confinement platforms using the same strain-induced change in effective refractive index report VLP values of approximately $50.7 \text{ V} \cdot \text{dB}$ [1] with propagation losses of 35 – 100 dB/m. Another high-confinement platform that relies on strain-induced optical path length modulation achieves a VLP of $22 \text{ V} \cdot \text{dB}$ [2]. Our low-confinement platform can leverage this same optical path length modulation

mechanism by fully releasing selected SPS sections to further reduce VLP (see Supplementary Fig. 1a and Fig. 1b). As shown in Supplementary Fig. 1a, this approach could reduce $V_\pi L$ of the low-confinement platform by a factor of 5 – 10 \times relative to current devices, potentially lowering the VLP to $\sim 4 \text{ V} \cdot \text{dB}$ or below.

We estimate the impact of reduced loss in LPNP circuits through an example protocol for the on-demand generation of heralded Bell and GHZ states using a four-mode and eight-mode linear programmable nanophotonic processor [7, 30, 37]. For this analysis, we consider propagation loss in the phase shifters as the sole loss mechanism, assuming all other components are lossless. The loss per phase shifter, γ , is equal to the ratio of VLP to the maximum applied voltage (V_{max}). At $V_{\text{max}} = 20 \text{ V}$, our low-confinement waveguide platform (VLP $\sim 20 \text{ V} \cdot \text{dB}$) incurs a loss of $\sim 1 \text{ dB}$ per phase shifter, whereas a future low-confinement platform (shown in Fig. 4b and Supplementary Fig. 1) with $V_\pi L < 3 \text{ V} \cdot \text{m}$ (VLP $< 4 \text{ V} \cdot \text{dB}$) would suffer a loss of $< 0.2 \text{ dB}$ per phase shifter. Fig. 4a illustrates how this difference translates into the probability of successfully heralding quantum states in a lossy LPNP circuit with ideal detectors. The results indicate dramatic improvements in quantum-state generation efficiency: for Bell-state preparation in a four-mode LPNP circuit, the success probability increases by roughly two orders of magnitude for the lower phase-shifter loss, and for heralded four-mode GHZ states, the success probability improves by a factor of $\sim 10^8$. Details of the calculation supporting these results are provided in Supplementary Note 4 and Supplementary Fig. 5.

This low-loss, scalable architecture forms the essential hardware backbone for applications such as quantum routers [9], universal quantum photonic logic circuits [38, 39], on-chip quantum memories for heralded entanglement swapping [40], tunable low-power optical true-time delay lines [41], and post-selected heralded GHZ state generation [7, 37]. Furthermore, the platform’s ultra-low propagation loss and anneal-free, foundry-compatible fabrication process enable seamless integration of single-photon sources, modulators, and electronic control, paving the way for complex, scalable, and fully integrated quantum photonic systems on a single chip.

Materials and methods

Devices measurement

To characterize the devices, we drive the SPS using a Keysight 33500B function generator as a voltage source in combination with a Thorlabs BPA100 benchtop high-voltage piezo amplifier, which provides a noise bandwidth from 20 Hz to 100 kHz. We apply a 200 Hz ramp modulation signal to the SPS (Fig. 2c), sweeping the voltage up to 120 V. We perform S-parameter measurements using a Keysight P9374A vector network analyzer. We measure the holding power with a Keithley 2450 source-measure unit, as shown in Supplementary Fig. 4b.

Top-down imaging measurement

Fig. 3a shows the experimental setup used to measure waveguide loss with a top-down imaging technique. We capture images using an Allied Vision 1800 U-120c camera

(1280 × 960 pixels) equipped with a Navitar 12× UltraZoom Video Microscopy System and a Mitutoyo 5× microscope objective (MO). Because the low-confinement waveguides exhibit extremely low loss and therefore weak light scattering, we adjust the imaging parameters during acquisition to improve the signal-to-noise ratio. For the unetched waveguide, where we image a section of the 1.8 m-long spiral, we use a gamma correction of 0.5, a gain of 35 dB, and an exposure time of 8.03 ms. For the etched waveguide with an actuator, we set the gamma correction to 0.5, the gain to 38.3 dB, and the exposure time to 7.3 ms.

Acknowledgments

This material is based upon work supported by the U.S. Department of Energy, Office of Science, National Quantum Information Science Research Centers, Quantum Systems Accelerator.

Author contributions:

N.T.O. and M.E. conceived the work. M.M. wrote the manuscript. M.M., G.C., W.H., G.M.T., K.K., M.G., A.L., D.D., N.T.O., and M.E. contributed to the experiments, simulations, and data analysis. M.M., G.C., G.M.T., N.T.O. and M.E. contributed to the revision of the paper. All authors discussed the results and implications.

Competing interests:

The authors declare that they have no competing interests.

Data and materials availability:

The data and code that support the findings of this study are available from the corresponding author upon reasonable request. All data needed to evaluate the conclusions in the paper are present in the paper and/or the Supplementary Materials. Additional data related to this paper may be requested from the authors.

References

- [1] Dong, M., Clark, G., Leenheer, A.J., Zimmermann, M., Dominguez, D., Menssen, A.J., Heim, D., Gilbert, G., Englund, D., Eichenfield, M.: High-speed programmable photonic circuits in a cryogenically compatible, visible–near-infrared 200 nm CMOS architecture. *Nature Photonics* **16**(1), 59–65 (2022) <https://doi.org/10.1038/s41566-021-00903-x>
- [2] Dong, M., Heim, D., Witte, A., Clark, G., Leenheer, A.J., Dominguez, D., Zimmermann, M., Wen, Y.H., Gilbert, G., Englund, D., Eichenfield, M.: Piezo-optomechanical cantilever modulators for VLSI visible photonics. *APL Photonics* **7**(5), 051304 (2022) <https://doi.org/10.1063/5.0088424>

- [3] Dong, M., Zimmermann, M., Heim, D., Choi, H., Clark, G., Leenheer, A.J., Palm, K.J., Witte, A., Dominguez, D., Gilbert, G., Eichenfield, M., Englund, D.: Programmable photonic integrated meshes for modular generation of optical entanglement links. *npj Quantum Information* **9**(1), 42 (2023) <https://doi.org/10.1038/s41534-023-00708-6>
- [4] Palm, K.J., Dong, M., Golter, D.A., Clark, G., Zimmermann, M., Chen, K.C., Li, L., Menssen, A., Leenheer, A.J., Dominguez, D., Gilbert, G., Eichenfield, M., Englund, D.: Modular chip-integrated photonic control of artificial atoms in diamond waveguides. *Optica* **10**(5), 634–641 (2023) <https://doi.org/10.1364/OPTICA.486361>
- [5] Stanfield, P.R., Leenheer, A.J., Michael, C.P., Sims, R., Eichenfield, M.: Cmos-compatible, piezo-optomechanically tunable photonics for visible wavelengths and cryogenic temperatures. *Opt. Express* **27**(20), 28588–28605 (2019) <https://doi.org/10.1364/OE.27.028588>
- [6] Clark, G., Raniwala, H., Koppa, M., Chen, K., Leenheer, A., Zimmermann, M., Dong, M., Li, L., Wen, Y.H., Dominguez, D., Trusheim, M., Gilbert, G., Eichenfield, M., Englund, D.: Nanoelectromechanical control of spin–photon interfaces in a hybrid quantum system on chip. *Nano Letters* **24**(4), 1316–1323 (2024) <https://doi.org/10.1021/acs.nanolett.3c04301> PMID: 38227973
- [7] Bhatti, D., Barz, S.: Generating greenberger-horne-zeilinger states using multi-port splitters. *Physical Review A* **107**(3), 033714 (2023)
- [8] Kazanskiy, N.L., Butt, M.A., Khonina, S.N.: Optical computing: Status and perspectives. *Nanomaterials* **12**(13) (2022) <https://doi.org/10.3390/nano12132171>
- [9] Lee, Y., Bersin, E., Dahlberg, A., Wehner, S., Englund, D.: A quantum router architecture for high-fidelity entanglement flows in quantum networks. *npj Quantum Information* **8**(1), 75 (2022) <https://doi.org/10.1038/s41534-022-00582-8>
- [10] Ibrahim, M.I., Foy, C., Kim, D., Englund, D.R., Han, R.: Room-temperature quantum sensing in cmos: On-chip detection of electronic spin states in diamond color centers for magnetometry. In: 2018 IEEE Symposium on VLSI Circuits, pp. 249–250 (2018). <https://doi.org/10.1109/VLSIC.2018.8502329>
- [11] Rudolph, T.: Why i am optimistic about the silicon-photonics route to quantum computing. *APL photonics* **2**(3) (2017)
- [12] Bauters, J.F., Heck, M.J.R., John, D., Dai, D., Tien, M.-C., Barton, J.S., Leinse, A., Heideman, R.G., Blumenthal, D.J., Bowers, J.E.: Ultra-low-loss high-aspect-ratio si3n4 waveguides. *Opt. Express* **19**(4), 3163–3174 (2011) <https://doi.org/10.1364/OE.19.003163>

- [13] Hong, S., Zhang, L., Wang, Y., Zhang, M., Xie, Y., Dai, D.: Ultralow-loss compact silicon photonic waveguide spirals and delay lines. *Photon. Res.* **10**(1), 1–7 (2022) <https://doi.org/10.1364/PRJ.437726>
- [14] Bauters, J.F., Heck, M.J.R., John, D.D., Barton, J.S., Bruinink, C.M., Leinse, A., Heideman, R.G., Blumenthal, D.J., Bowers, J.E.: Planar waveguides with less than 0.1 db/m propagation loss fabricated with wafer bonding. *Opt. Express* **19**(24), 24090–24101 (2011) <https://doi.org/10.1364/OE.19.024090>
- [15] Jin, W., Yang, Q.-F., Chang, L., Shen, B., Wang, H., Leal, M.A., Wu, L., Gao, M., Feshali, A., Paniccia, M., Vahala, K.J., Bowers, J.E.: Hertz-linewidth semiconductor lasers using cmos-ready ultra-high-q microresonators. *Nature Photonics* **15**(5), 346–353 (2021) <https://doi.org/10.1038/s41566-021-00761-7>
- [16] Chauhan, N., Isichenko, A., Wang, J., Blumenthal, D.J.: Sub-db/m loss integrated 103 and 90 million q resonators for laser stabilization at rubidium and strontium wavelengths. In: 2022 IEEE Photonics Conference (IPC), pp. 1–2 (2022). <https://doi.org/10.1109/IPC53466.2022.9975529>
- [17] Chauhan, N., Wang, J., Bose, D., Liu, K., Compton, R.L., Fertig, C., Hoyt, C.W., Blumenthal, D.J.: Ultra-low loss visible light waveguides for integrated atomic, molecular, and quantum photonics. *Opt. Express* **30**(5), 6960–6969 (2022) <https://doi.org/10.1364/OE.448938>
- [18] Blumenthal, D.J.: Photonic integration for UV to IR applications. *APL Photonics* **5**(2), 020903 (2020) <https://doi.org/10.1063/1.5131683>
- [19] Blumenthal, D.J., Heideman, R., Geuzebroek, D., Leinse, A., Roeloffzen, C.: Silicon nitride in silicon photonics. *Proceedings of the IEEE* **106**(12), 2209–2231 (2018) <https://doi.org/10.1109/JPROC.2018.2861576>
- [20] Isichenko, A., Hunter, A.S., Bose, D., Chauhan, N., Song, M., Liu, K., Harrington, M.W., Blumenthal, D.J.: Sub-hz fundamental, sub-khz integral linewidth self-injection locked 780 nm hybrid integrated laser. *Scientific Reports* **14**(1), 27015 (2024) <https://doi.org/10.1038/s41598-024-76699-x>
- [21] Isichenko, A., Chauhan, N., Bose, D., Wang, J., Kunz, P.D., Blumenthal, D.J.: Photonic integrated beam delivery for a rubidium 3d magneto-optical trap. *Nature Communications* **14**(1), 3080 (2023) <https://doi.org/10.1038/s41467-023-38818-6>
- [22] Chauhan, N., Isichenko, A., Liu, K., Wang, J., Zhao, Q., Behunin, R.O., Rakich, P.T., Jayich, A.M., Fertig, C., Hoyt, C.W., Blumenthal, D.J.: Visible light photonic integrated brillouin laser. *Nature Communications* **12**(1), 4685 (2021) <https://doi.org/10.1038/s41467-021-24926-8>
- [23] Chanana, A., Larocque, H., Moreira, R., Carolan, J., Guha, B., Melo, E.G.,

- Anant, V., Song, J., Englund, D., Blumenthal, D.J., Srinivasan, K., Davanco, M.: Ultra-low loss quantum photonic circuits integrated with single quantum emitters. *Nature Communications* **13**(1), 7693 (2022) <https://doi.org/10.1038/s41467-022-35332-z>
- [24] Yong, Z., Chen, H., Luo, X., Govdeli, A., Chua, H., Azadeh, S.S., Stalmashonak, A., Lo, G.-Q., Poon, J.K.S., Sacher, W.D.: Power-efficient silicon nitride thermo-optic phase shifters for visible light. *Opt. Express* **30**(5), 7225–7237 (2022) <https://doi.org/10.1364/OE.448614>
- [25] Liu, K., Chauhan, N., Song, M., Harrington, M.W., Nelson, K.D., Blumenthal, D.J.: Tunable broadband two-point-coupled ultra-high-q visible and near-infrared photonic integrated resonators. *Photon. Res.* **12**(9), 1890–1898 (2024) <https://doi.org/10.1364/PRJ.528398>
- [26] Hosseini, N., Dekker, R., Hoekman, M., Dekkers, M., Bos, J., Leinse, A., Heideman, R.: Stress-optic modulator in triplex platform using a piezoelectric lead zirconate titanate (pzt) thin film. *Opt. Express* **23**(11), 14018–14026 (2015) <https://doi.org/10.1364/OE.23.014018>
- [27] Wang, J., Liu, K., Harrington, M.W., Rudy, R.Q., Blumenthal, D.J.: Silicon nitride stress-optic microresonator modulator for optical control applications. *Opt. Express* **30**(18), 31816–31827 (2022) <https://doi.org/10.1364/OE.467721>
- [28] Montifiore, N., Isichenko, A., Chauhan, N., Wang, J., Hunter, A.S., Harrington, M.W., Chawhani, R., Rudy, R.Q., Kierzewski, I., Pushkarsky, M., Blumenthal, D.J.: Blue to Near-IR Integrated PZT Silicon Nitride Modulators for Quantum and Atomic Applications (2026). <https://arxiv.org/abs/2601.15695>
- [29] Tian, H., Liu, J., Attanasio, A., Siddharth, A., Blésin, T., Wang, R.N., Voloshin, A., Lihachev, G., Riemensberger, J., Kenning, S.E., Tian, Y., Chang, T.H., Bancora, A., Snigirev, V., Shadymov, V., Kippenberg, T.J., Bhave, S.A.: Piezoelectric actuation for integrated photonics. *Adv. Opt. Photon.* **16**(4), 749–867 (2024) <https://doi.org/10.1364/AOP.529288>
- [30] Clements, W.R., Humphreys, P.C., Metcalf, B.J., Kolthammer, W.S., Walmsley, I.A.: Optimal design for universal multiport interferometers. *Optica* **3**(12), 1460–1465 (2016) <https://doi.org/10.1364/OPTICA.3.001460>
- [31] Gyger, F., Liu, J., Yang, F., He, J., Raja, A.S., Wang, R.N., Bhave, S.A., Kippenberg, T.J., Thévenaz, L.: Observation of stimulated brillouin scattering in silicon nitride integrated waveguides. *Phys. Rev. Lett.* **124**, 013902 (2020) <https://doi.org/10.1103/PhysRevLett.124.013902>
- [32] Dong, M., Boyle, J.M., Palm, K.J., Zimmermann, M., Witte, A., Leenheer, A.J., Dominguez, D., Gilbert, G., Eichenfield, M., Englund, D.: Synchronous micromechanically resonant programmable photonic circuits. *Nature Communications*

14(1), 7716 (2023) <https://doi.org/10.1038/s41467-023-42866-3>

- [33] Chiu, C., Liao, Y.-H.: The critical adiabatic linear tapered waveguide combined with a multimode waveguide coupler on an soi chip. *International Journal of Optics* **2019**(1), 4270612 (2019)
- [34] Dixon, R.W.: Photoelastic Properties of Selected Materials and Their Relevance for Applications to Acoustic Light Modulators and Scanners. *Journal of Applied Physics* **38**(13), 5149–5153 (1967) <https://doi.org/10.1063/1.1709293>
- [35] Corato-Zanarella, M., Ji, X., Mohanty, A., Lipson, M.: Absorption and scattering limits of silicon nitride integrated photonics in the visible spectrum. *Opt. Express* **32**(4), 5718–5728 (2024) <https://doi.org/10.1364/OE.505892>
- [36] Jaber, N., Madaras, S., Starbuck, A., Pomerene, A., Dallo, C., Trotter, D.C., Gehl, M., Otterstrom, N.: Non-resonant bragg scattering four-wave mixing at near-visible wavelengths in low-confinement silicon nitride waveguides. *Opt. Lett.* **49**(11), 3146–3149 (2024) <https://doi.org/10.1364/OL.519793>
- [37] Bhatti, D., Barz, S.: Heralding higher-dimensional bell and greenberger–horne–zeilinger states using multiport splitters. *New Journal of Physics* **27**(3), 033006 (2025)
- [38] Taballione, C., Meer, R., Snijders, H.J., Hooijschuur, P., Epping, J.P., Goede, M., Kassenberg, B., Venderbosch, P., Toebes, C., Vlekkert, H., Pinkse, P.W.H., Renema, J.J.: A universal fully reconfigurable 12-mode quantum photonic processor. *Materials for Quantum Technology* **1**(3), 035002 (2021) <https://doi.org/10.1088/2633-4356/ac168c>
- [39] Carolan, J., Harrold, C., Sparrow, C., Martín-López, E., Russell, N.J., Silverstone, J.W., Shadbolt, P.J., Matsuda, N., Oguma, M., Itoh, M., Marshall, G.D., Thompson, M.G., Matthews, J.C.F., Hashimoto, T., O’Brien, J.L., Laing, A.: Universal linear optics. *Science* **349**(6249), 711–716 (2015) <https://doi.org/10.1126/science.aab3642>
- [40] Dhara, P., Englund, D., Guha, S.: Entangling quantum memories via heralded photonic bell measurement. *Phys. Rev. Res.* **5**, 033149 (2023) <https://doi.org/10.1103/PhysRevResearch.5.033149>
- [41] Ji, X., Yao, X., Gan, Y., Mohanty, A., Tadayon, M.A., Hendon, C.P., Lipson, M.: On-chip tunable photonic delay line. *APL Photonics* **4**(9), 090803 (2019) <https://doi.org/10.1063/1.5111164>

Supplementary Information

Ultra-low loss piezo-optomechanical low-confinement silicon nitride platform for visible wavelength quantum photonic circuits

Mayank Mishra¹, Gwangho Choi¹, Wenhua He¹, Gina M. Talcott², Katherine Kearney², Michael Gehl², Andrew Leenheer², Daniel Dominguez², Nils T. Otterstrom^{2*}, Matt Eichenfield^{1,2,3*}

¹ James C. Wyant College of Optical Sciences, University of Arizona, Tucson, Arizona 85721, USA

² Microsystems Engineering, Science, and Applications, Sandia National Laboratories, Albuquerque, New Mexico 87185, USA

³ Electrical, Computer and Energy Engineering, University of Colorado, Boulder, Colorado 80309, USA

*Correspondence to: ntotter@sandia.gov; Matt.Eichenfield@colorado.edu

Contents

1 Comparison table for visible wavelength low-confinement silicon nitride waveguide pic platforms	2
2 Strain-induced change in effective refractive index and estimation of photoelastic coefficients of silicon nitride	3
2.1 Estimation of silicon nitride photoelastic coefficients $p_{11} = -0.125$ and $p_{12} = 0.047$	5
2.2 Voltage-length product ($V_{\pi}L$) of other devices	7
3 Heralded Bell state and 4-mode GHZ state generation using lossy LPNP circuit	7
4 Propagation loss measurements	10
4.1 Top-down imaging measurement	10
4.2 Direct transmission measurement	11
4.3 Optical time-domain reflectometry (OTDR)	11
5 Loss-responsivity trade-off	12
6 Scattering loss model	12
6.1 3D loss model	12
6.2 2D loss model	14
7 Optimal waveguide geometry for minimum VLP with silicon nitride piezo-optic coefficients $p_{11} = -0.125$ and $p_{12} = 0.047$	16

1 Comparison table for visible wavelength low-confinement silicon nitride waveguide pic platforms

Material	Fabrication Method	Wavelength (nm)	Propagation Loss (dB/cm)	voltage-loss (V · dB)	Product	References
Silicon Nitride	LPCVD ¹	405	0.93	N/A (passive)		[1]
Silicon Nitride	LPCVD	450	0.22	N/A (passive)		[1]
Silicon Nitride	LPCVD	450	0.35	N/A (passive)		[1]
Silicon Nitride	LPCVD	461	0.09	N/A (passive)		[2]
Silicon Nitride	LPCVD	802	0.02	N/A (passive)		[2]
Silicon Nitride	LPCVD	674	0.01	N/A (passive)		[2]
Silicon Nitride	LPCVD	698	0.03	N/A (passive)		[2]
Silicon Nitride	LPCVD	450	0.08	N/A (passive)		[2]
Silicon Nitride	LPCVD	930	0.01	N/A (passive)		[3]
Silicon Nitride	LPCVD	654	0.25	N/A (passive)		[4]
Silicon Nitride	LPCVD	780	4.85	N/A (passive)		[5]
Silicon Nitride	LPCVD	602-648	0.5-1.4	N/A (passive)		[6]
Silicon Nitride	PECVD ²	602-648	1.3-2.4	N/A (passive)		[6]
Silicon Nitride	PECVD	430-464	2.5-4.5	N/A (passive)		[6]
Silicon Nitride	PECVD	466-500	2.2-2.8	N/A (passive)		[6]
Silicon Nitride	PECVD	502-550	1.5-2.4	N/A (passive)		[6]
Silicon Nitride	PECVD	555-600	1.3-1.6	N/A (passive)		[6]
Silicon Nitride	PECVD	668	5.7	N/A (passive)		[7]
Silicon Nitride	LPCVD	938	0.6	N/A (passive)		[7]
Silicon Nitride	LPCVD	780	0.46	N/A (passive)		[8]
Silicon Nitride	LPCVD	780	0.73	N/A		[9]
Silicon Nitride	PECVD	900	0.3	N/A (passive)		[10]
Silicon Nitride	PECVD	780	1.33	N/A (passive)		[10]
Silicon Nitride	PECVD	532	0.65	N/A (passive)		[10]
Silicon Nitride	PECVD	600	0.51	N/A (passive)		[11]
Silicon Nitride	LPCVD	780	0.043	1.3		[12]
Silicon Nitride	PECVD	780	0.39	50.7 (Active, high-confinement)	high-	[13]
Silicon Nitride	PECVD	737	0.38	22 (Active, high-confinement)	high-	[14]
Silicon Nitride	PECVD	737	0.51	36 (Active, high-confinement)	high-	[14]
Silicon Nitride	LPCVD	780	0.043	N/A (passive)		[15]
Silicon Nitride	LPCVD	780	0.0175	N/A (passive)		[16]
Silicon Nitride	LPCVD	780	0.015	N/A (passive)		[17]
Silicon Nitride		780	0.27	2.34		[31]
Silicon Nitride	PECVD	780	0.0257	passive		This work
Silicon Nitride	PECVD	780	0.072	19.4		This work

Table 1 Performance comparison of low-confinement silicon nitride platforms (to the best of our current knowledge).

¹ LPCVD: Low-pressure chemical vapor deposition

² PECVD: Plasma-enhanced chemical vapor deposition

Table 1 presents a comprehensive summary of the propagation loss and voltage-loss product (VLP) for low-confinement silicon nitride waveguide photonic devices designed for operation in the 400 nm–1000 nm wavelength band. As shown in Fig. 1, our platform achieves the lowest propagation loss among all silicon nitride platforms fabricated using PECVD deposition processes.

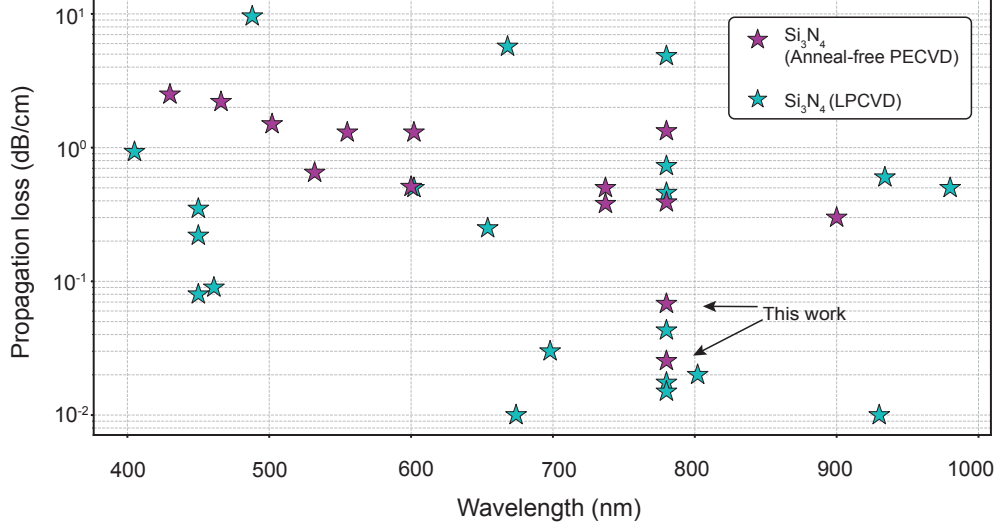


Fig. 1 Summary of propagation loss values from Table 1 for silicon nitride waveguide photonic devices, covering wavelengths from 400 nm–1000 nm.

2 Strain-induced change in effective refractive index and estimation of photoelastic coefficients of silicon nitride

The phase shift $\Delta\theta$ experienced by an optical mode propagating through a phase shifter of length L under an applied strain can be expressed as

$$\Delta\theta = \frac{2\pi}{\lambda}(\Delta n_{\text{eff}}L + n_{\text{eff}}\Delta L), \quad (2)$$

where λ denotes the free-space wavelength, n_{eff} is the effective refractive index, and ΔL is the strain-induced change in the optical path length [14]. In this low-confinement waveguide platform, the contribution from ΔL is negligible compared to the refractive index modulation. If, however, a few sections of the SPS are fully released, $V_{\pi}L$ could in principle be reduced by a factor of 5 – 10 compared to the value measured in our current devices as shown in Fig. 2a and 2b.

The parameter Δn_{eff} encapsulates the total strain-induced change in effective refractive index, expressed as

$$\Delta n_{\text{eff}} = \Delta n_{\text{eff,PE}} + \Delta n_{\text{eff,MB}}. \quad (3)$$

Here, $\Delta n_{\text{eff,PE}}$ quantifies the photoelastic effect, and $\Delta n_{\text{eff,MB}}$ quantifies the moving boundary effect. FEM simulations for our platform reveal that the photoelastic contribution is on the order of 10^{-7}V^{-1} , whereas the moving boundary contribution is on the order of 10^{-9}V^{-1} as shown in Fig. 2 c.

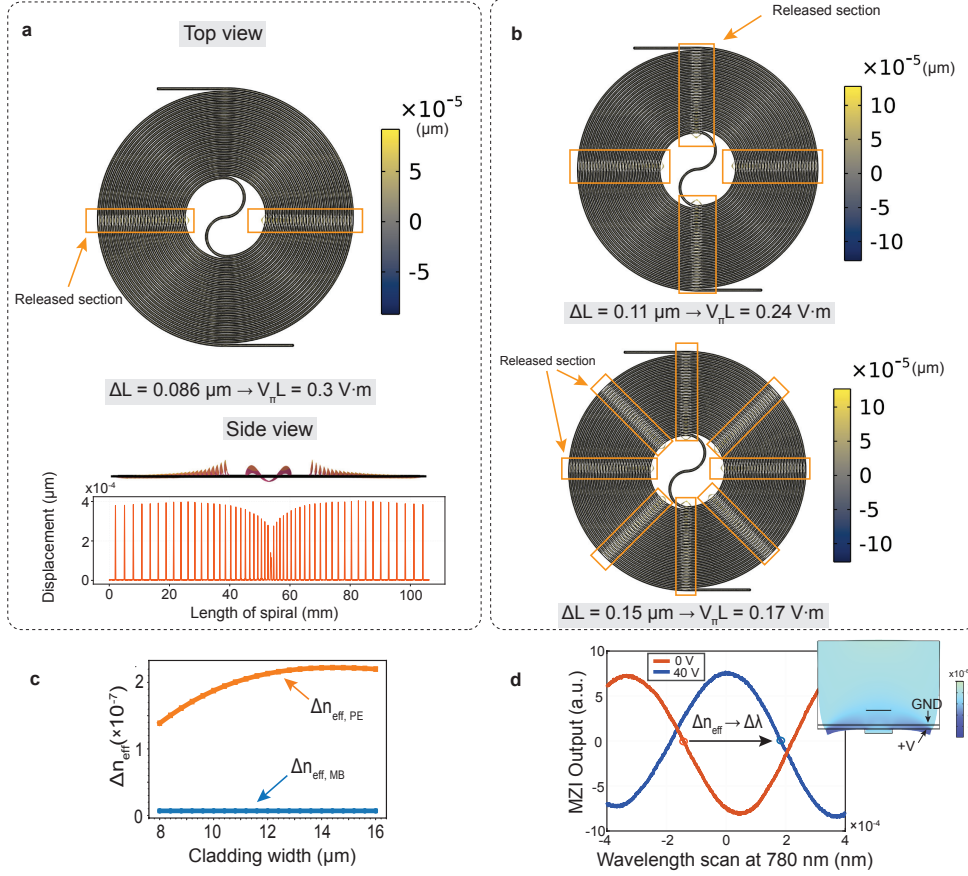


Fig. 2 Strain-induced deformation and photoelastic refractive-index modulation in SPS waveguides: schematics, simulations, and wavelength shift experimental result.

a Top- and side-view schematics illustrate the (exaggerated) strain-induced deformation of the released SPS section under an applied voltage. The accompanying plot presents the simulated displacement of the cladding edge along the spiral length. **b** A top-view schematic illustrates the exaggerated strain-induced deformation of the 4- and 8-released SPS sections under an applied voltage. The $V_{\pi}L$ reaches values as low as 0.17 V·m. **c** FEM simulation of the strain-induced change in effective refractive index, showing that the photoelastic (PE) contribution ($\sim 10^{-7}/V$) exceeds the moving boundary (MB) contribution ($\sim 10^{-9}/V$) for different cladding widths. **d** Measured fringe shift when 40 V is applied to the SPS in MZI while scanning the laser wavelength at 780 nm, indicating a positive effective refractive index change under negative strain. This is possible only for the case when the dominant photoelastic contribution in these low-confinement waveguides comes from the silicon oxide cladding.

The strain-induced change in the refractive index tensor component Δn_{ij} is related to the strain tensor components s_{kl} as

$$\Delta n_{ij} \propto - \sum_{k,l} p_{ijkl} s_{kl}. \quad (4)$$

Here p_{ijkl} is the photoelastic tensor. An applied electric field in aluminum nitride induces strain according to

$$s_{kl} = \sum_m d_{klm} E_m. \quad (5)$$

The relevant AlN piezoelectric coupling tensor components are $d_{33} \approx 5$ pm/V, $d_{31} \approx -2$ pm/V [32], and $d_{15} \approx -2$ pm/V. In these devices, the d_{31} component primarily determines the piezoelectric response, as the actuator's electric fields are nearly vertical ($E_m \approx \Delta V/t_{AlN}$, with t_{AlN} being the AlN layer thickness).

2.1 Estimation of silicon nitride photoelastic coefficients

$$p_{11} = -0.125 \text{ and } p_{12} = 0.047$$

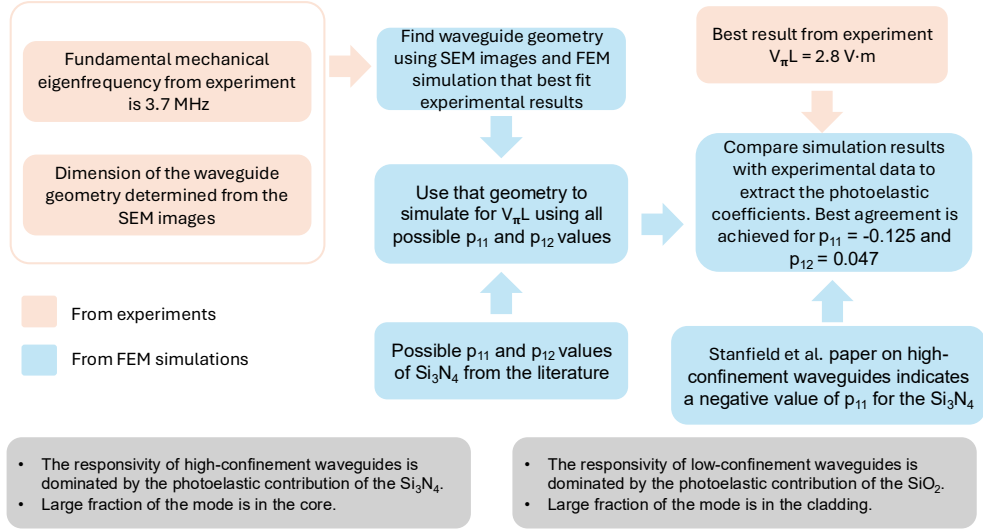


Fig. 3 Simulation workflow for the estimation of silicon nitride photoelastic coefficients. The simulation incorporates actual waveguide dimensions to identify the best-fit parameters $p_{11} = -0.125$ and $p_{12} = 0.047$

The photoelastic coefficients used in our initial simulation while designing devices and in results shown in Fig. 2c are as follows: for silicon nitride, $p_{11} = 0.1$ (assumed), $p_{12} = 0.047$ (assumed) [26, 28], and $p_{44} = 0.5(p_{11} - p_{12}) = 0.0265$; for silicon dioxide, $p_{11} = 0.121$, $p_{12} = 0.27$, and $p_{44} = 0.5(p_{11} - p_{12}) = -0.0745$ [28]. In the FEM simulations, we use a refractive index of 1.92 for silicon nitride and 1.45 for silicon dioxide.

The reported values for silicon nitride photoelastic coefficients are $|p_{12}| = 0.047 \pm 0.004$ and $|p_{44}| = 0.086$ [26, 28]. Based on these values, there are four possible sign combinations for p_{11} , corresponding to the two magnitudes $|0.125|$ and $|0.219|$.

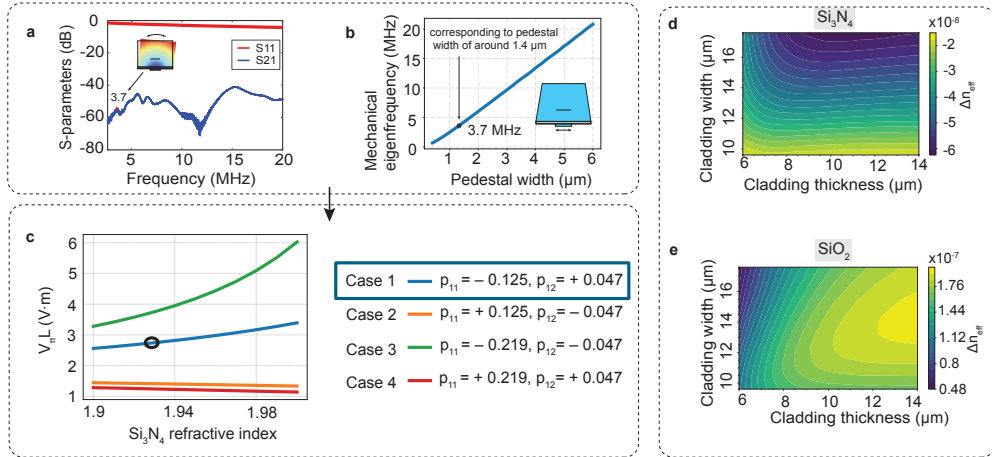


Fig. 4 Photoelastic coefficient determination through mechanical, optical characterization and FEM simulation.

a Measured S11 and S21 responses of the SPS, showing a fundamental mechanical resonance at approximately 3.7 MHz. **b** FEM-derived relationship between waveguide pedestal width and mechanical eigenfrequency; a resonance at 3.7 MHz corresponds to a pedestal width of $\approx 1.4 \mu\text{m}$. **c** FEM-simulated $V_{\pi}L$ values for geometry with pedestal width of $\approx 1.4 \mu\text{m}$, evaluated for four combinations of silicon nitride photoelastic coefficients and refractive indices. The parameter set $p_{11} = -0.125$ and $p_{12} = 0.047$ provides the best agreement with the experimental data for Si_3N_4 refractive index of 1.93. **d** Simulated change in effective refractive index per applied voltage using silicon nitride photoelastic coefficients ($p_{11} = -0.125$, $p_{12} = 0.047$) with silicon dioxide photoelastic coefficients set to zero, resulting in a negative $\Delta n_{\text{eff}}/V$. **e** Corresponding simulation using only silicon dioxide photoelastic coefficients ($p_{11} = 0.121$, $p_{12} = 0.27$), showing a positive and an order of magnitude larger $\Delta n_{\text{eff}}/V$, indicating a dominant PE effect in SiO_2 and an opposing influence from Si_3N_4 .

We estimate the waveguide cross-sectional dimensions from the SEM images in Fig. 2a and Fig. 2b. We extract the pedestal width of $1.4 \mu\text{m}$ from mechanical resonance measurements (see Fig. 4a) and FEM simulation (see 4b). Using these geometric parameters, we run FEM simulations to compute $V_{\pi}L$ for the four cases, shown in Fig. 4c. Among them, only the combination $p_{11} = -0.125$ and $p_{12} = 0.047$ of silicon nitride yields values that closely match our experimental measured value of $V_{\pi}L = 2.8 V \cdot m$. This observation aligns with results reported for high-confinement waveguides in Ref. [25], where the resonance frequency of a ring resonator decreases under applied positive strain, indicating the change in effective refractive index is positive that is possible if p_{11} is negative. The workflow for this estimation procedure is summarized in Fig. 3.

When we use $p_{11} = -0.125$ and $p_{12} = 0.047$ for silicon nitride and set the photoelastic coefficients of silicon dioxide (p_{11} and p_{12}) to zero, the simulated change in the effective refractive index per applied voltage, as shown in Fig. 4d, is negative with respect to changes in the cladding width and thickness. Conversely, when we set the photoelastic coefficients of silicon nitride to zero and use $p_{11} = 0.121$ and $p_{12} = 0.27$ for silicon dioxide, the change in the effective refractive index per applied voltage becomes positive and an order of magnitude larger, as shown in Fig. 4e. These results

indicate that silicon dioxide exerts a dominant influence on the voltage-induced change in refractive index because a large fraction of the optical mode resides in the cladding, whereas the silicon nitride core contributes an opposite, smaller effect. This observation agrees with the experimentally measured wavelength shift of the MZI when negative strain is applied to the SPS, as shown in Fig. 2d.

2.2 Voltage-length product ($V_\pi L$) of other devices

To characterize the devices, we use a function generator as voltage source in combination with a Thorlabs BPA100 benchtop high-voltage piezo amplifier, which provides a noise bandwidth of 20 Hz to 100 kHz. Fig. 5a shows the on-chip Mach–Zehnder interferometer operating in a differential configuration, with the inset displaying a micrograph of the on-chip MZI. We apply a 200 Hz ramp modulation signal, sweeping the voltage from approximately -20 V to 40 V and up to 120 V, depending on the test condition. Fig. 5b presents the holding power as a function of applied voltage (0–10 V) for the SPS reported in the main text, showing a holding power of 0.25 nW at an actuator bias of 5 V. Fig. 5c shows the same SPS response reported in the main text (Fig. 2). Fig. 5d and e display the optical responses of two additional MZI devices incorporating ~ 9.8 cm-long Archimedean SPSs in a push–pull configuration, with measured V_π values of approximately 40 V.

3 Heralded Bell state and 4-mode GHZ state generation using lossy LPNP circuit

In this calculation, we assume that the dominant loss in the unit cell (Fig. 6a) of the LPNP circuit is the propagation loss of the phase shifters, while all other components are considered lossless. As described in the discussion section of the paper, we consider two loss cases of the phase shifter $\gamma = 1$ dB/m, and $\gamma = 0.2$ dB/m. To simplify the analysis, we model the loss in each phase shifter as a beam splitter with transmissivity $\sqrt{\eta}$ on each arm. Since these beam splitters have equal losses on both arms, they commute with other beam splitters and single-mode phase shifters within the unit cell. Therefore, a lossy unit cell with beam splitters next to phase shifters is equivalent to a lossy unit cell with beam splitters concentrated at the input, as shown in Fig. 6b. To convert phase shifter loss γ into linear transmissivity, we employ the following equation:

$$\eta = (10^{-\gamma/10})^2. \quad (6)$$

For $\gamma = 0.2$ dB/m, this yields $\eta_{LC} = 0.91$, while for $\gamma = 1$ dB/m, $\eta_{HC} = 0.63$.

We adopt the GHZ state heralding protocol outlined in [18] to assess the success probability for on-demand generation of Bell and 4-mode GHZ states via a lossy PIC. For heralded Bell state generation, two pairs of indistinguishable single photons occupying orthogonal internal degrees of freedom ($D \in \{\alpha, \beta\}$) are used and passed through a 4-mode PIC, as illustrated in Fig. 6c. The input state to the 4-mode PIC

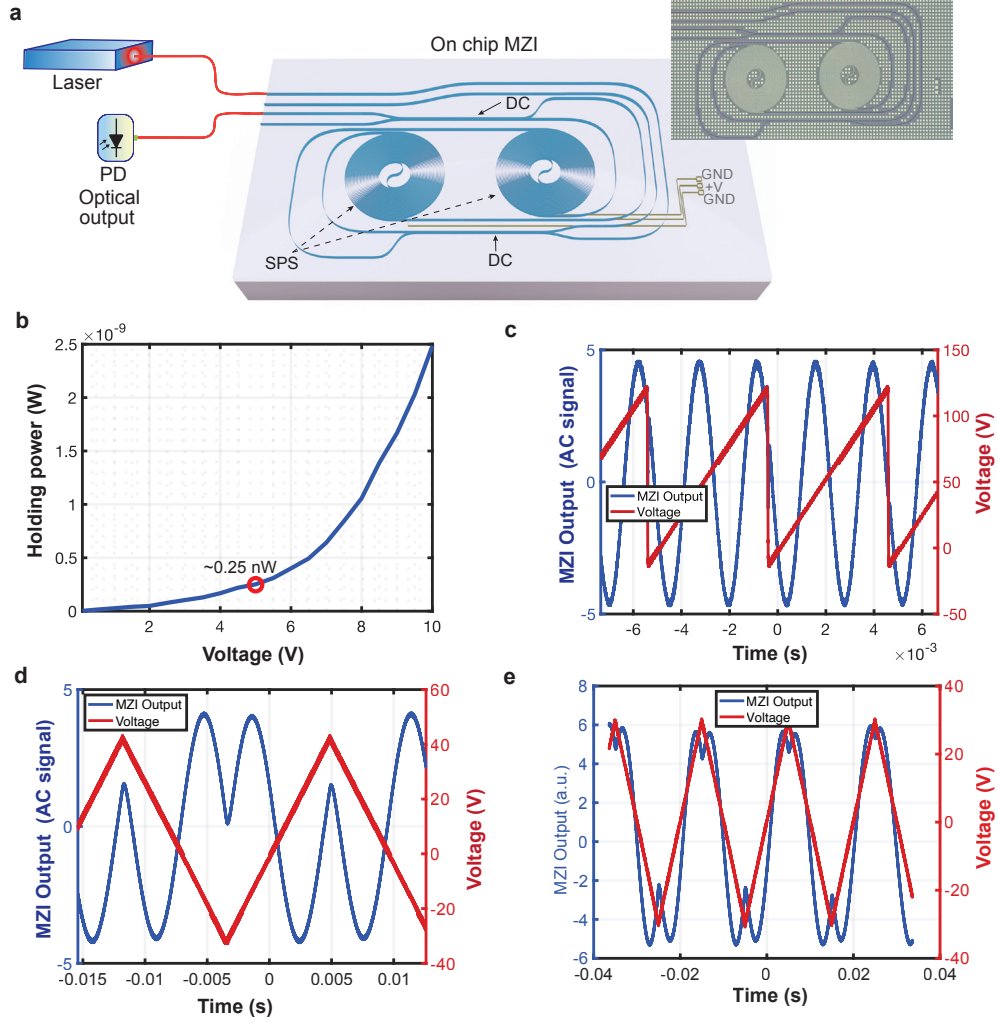


Fig. 5 On-chip MZI and SPS characterization.

a Schematic of the on-chip Mach-Zehnder interferometer operating in a differential configuration, with inset showing a micrograph of the fabricated device. **b** Measured holding power as a function of applied voltage for the SPS, showing 0.25 nW holding power at a 5 V actuator bias. **c** Optical response of the same SPS corresponding to the device reported in Fig. 2. **d, e** Optical responses of two additional MZI devices incorporating ~ 9.8 cm-long Archimedean SPSs in a push-pull configuration.

is given by

$$|\Psi_{4,\text{in}}\rangle = \prod_{k=1}^4 a_{D,k}^\dagger |0\rangle = |1\rangle_{\alpha,1} \otimes |1\rangle_{\beta,2} \otimes |1\rangle_{\alpha,3} \otimes |1\rangle_{\beta,4} \equiv |\alpha\rangle_1 |\beta\rangle_2 |\alpha\rangle_3 |\beta\rangle_4 \quad (7)$$

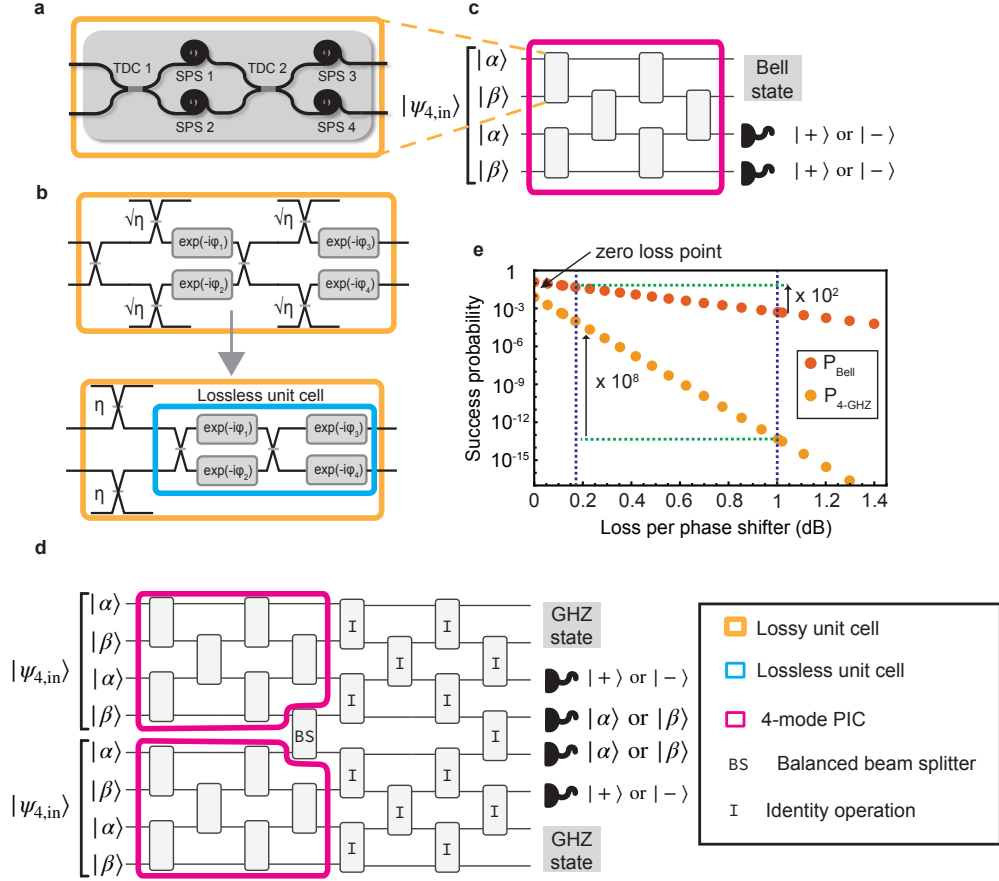


Fig. 6 Impact of phase-shifter loss on heralded Bell and GHZ state generation in LPNP photonic circuits.

a Lossy unit cell of an LPNP circuit consists of two tunable directional couplers and four spiral phase shifters. **b** We simulate the phase shifter losses in a lossy unit cell by employing beam splitters with transmissivity $\sqrt{\eta}$ that interact with a vacuum mode representing the environment. **c**, **d** show 4-mode and 8-mode PICs initialized with the input state $|\Psi_{4,\text{in}}\rangle$ to herald the generation of Bell and 4-mode GHZ states. **e** Probability of heralding Bell and GHZ states for these protocols in the presence of losses.

where $a_{D,k}^\dagger$ ($a_{D,k}$) denotes the creation (annihilation) operator for a photon in the k th spatial input mode with internal degree of freedom $D \in \{\alpha, \beta\}$, and $|n\rangle_{D,k}$ denotes the corresponding Fock state.

The unitary transformation U maps the 4-mode input state to a 4-mode output state using a 4-port PIC, with matrix elements U_{kl} ($k, l = 1, 2, 3, 4$), mapping input creation operators $a_{D,k}^\dagger$ to output creation operators $b_{D,l}^\dagger$ as follows:

$$a_{D,k}^\dagger \rightarrow \sum_{l=1}^4 U_{kl} b_{D,l}^\dagger, \quad (8)$$

$$U_{kl} = \frac{1}{\sqrt{4}} \omega^{(k-1)(l-1)}. \quad (9)$$

where $\omega = \exp(i2\pi/4)$. To account for loss within the unitary transformation, we decompose the unitary matrix into a Clements mesh [19] and introduce equal loss to each arm of the unit cell, as illustrated in Fig. 6b.

Heralding of Bell states in the first and second modes is achieved by performing temporal mode-resolving photon-number-resolving detection (PNRD) [18] on the third and fourth output modes. The specific click patterns associated with these heralded Bell states are:

$$|+\rangle_3|+\rangle_4 \text{ and } |-\rangle_3|-\rangle_4 \rightarrow \frac{1}{\sqrt{2}}(|\alpha\rangle_1|\alpha\rangle_2 - |\beta\rangle_1|\beta\rangle_2) \quad (10)$$

$$|+\rangle_3|-\rangle_4 \text{ and } |-\rangle_3|+\rangle_4 \rightarrow \frac{1}{\sqrt{2}}(|\alpha\rangle_1|\alpha\rangle_2 + |\beta\rangle_1|\beta\rangle_2) \quad (11)$$

where $|+\rangle = (|\alpha\rangle + |\beta\rangle)/\sqrt{2}$ and $|-\rangle = (|\alpha\rangle - |\beta\rangle)/\sqrt{2}$ are the rotated basis states used for mode-resolving measurements. In the lossless limit, the probability of success is 0.125, as shown in Fig. 6e. With the detection of the click patterns shown in Eqs. 10 and 11, a Bell state in the corresponding form is successfully heralded with fidelity of 1. We evaluated the probability of success for this protocol in the presence of losses, utilizing the models depicted in Fig. 6b and 6c, in which we monitor the same specified click pattern. The probability of success of the protocol in the presence of losses is shown in Fig. 6e. This protocol can be scaled up by stacking larger-mode PICs and performing the corresponding measurements at the appropriate output ports.

For example, the heralded 4-mode GHZ state preparation protocol employs 8-mode PICs, initialized with two $|\Psi_{4,\text{in}}\rangle$ states. The two 4-mode PICs in the 8-mode PIC are interconnected via a balanced beam splitter to interfere the fourth and fifth modes, as shown in Fig. 6d. By applying Clements' decomposition to the unitary transformation, we determine the contribution of each lossy unit cell within the 8-mode PIC, half of which are identity operations. Heralding a 4-mode GHZ state in the first, second, seventh, and eighth output ports involves specific measurements on the third, fourth, fifth, and sixth modes, performed in the original and rotated bases, respectively. In the ideal case without losses, this state can be heralded with a probability of 1/128, with a deterministic click pattern indicating successful preparation (as detailed in [18]), while Fig. 6e illustrates the heralded probability in the presence of losses.

4 Propagation loss measurements

4.1 Top-down imaging measurement

Fig. 3a presents the experimental setup for measuring waveguide loss using the top-down imaging technique. We capture images with an Allied Vision 1800 U-120c camera (1,280 × 960 pixels), equipped with a Navitar 12× UltraZoom Video Microscopy System and a Mitutoyo 5× microscope objective (MO). Because the low-confinement waveguides exhibit very low loss and therefore minimal light scattering, we adjust

the imaging parameters during acquisition to improve the signal-to-noise ratio. For the unetched waveguide, where we image a section of the long spiral 1.8 m, we use the following postprocessing parameters: gamma correction = 0.5, gain = 35 dB, and exposure time = 8.03 ms. For the etched waveguide with actuator, we set the parameters to gamma correction = 0.5, gain = 38.3 dB, and exposure time = 7.3 ms.

4.2 Direct transmission measurement

Direct transmission measurements of low-confinement silicon nitride waveguides were performed using spiral waveguides with lengths of 5 cm, 10 cm, and 180 cm to quantify propagation loss at 780 nm. We measured the optical power transmitted through each device and generated a linear fit of the normalized transmitted power versus the length of the waveguide, as shown in Fig. 7a. This fit yields a propagation loss coefficient of 3.87 dB/m and an insertion loss of 1.9 dB per input/output facet.

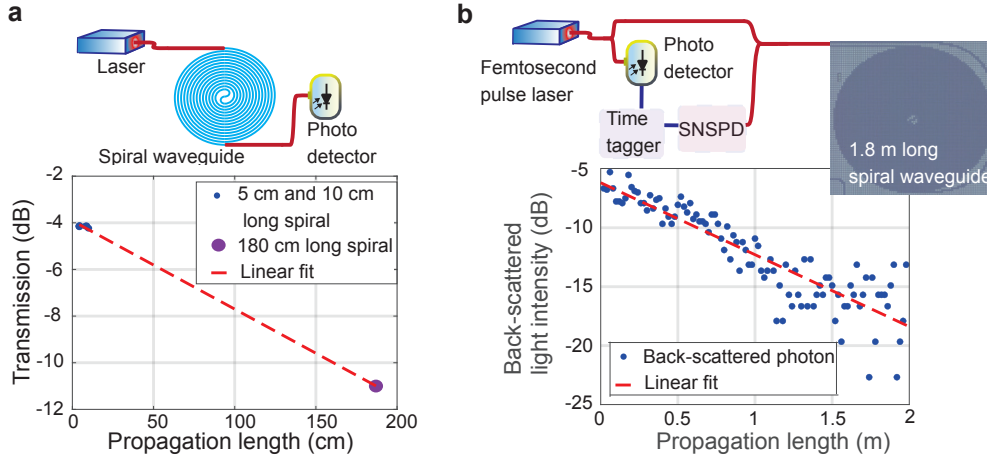


Fig. 7 Waveguide loss measurements using direct transmission and OTDR. **a** Direct transmission measurements of propagation loss using waveguides of 5 cm, 10 cm, and 180 cm lengths. Linear fit reveals a loss of 3.87 dB/m. **b** Optical time-domain reflectometry (OTDR) for loss characterization, utilizing a femtosecond laser, a time-tagger with a fast detector for pulse triggering, and an avalanche photodiode (APD). Linear fit indicates a loss of 6.1 dB/m.

4.3 Optical time-domain reflectometry (OTDR)

The experiment employs femtosecond laser-based optical time-domain reflectometry [3] to characterize propagation loss in a 1.8 m silicon nitride spiral waveguide. A Ti:sapphire femtosecond laser operating at 800 nm generates 180 fs pulses at a 1 kHz repetition rate. The laser light is injected into the waveguide by first coupling the free-space beam into a single-mode fiber, which is then coupled to the waveguide using a fiber array. Backscattered photons from Rayleigh scattering and localized defects are detected using a single-photon avalanche diode (APD) with 22 ns dead time,

synchronized using a fast photodetector via a time tagger triggered by the laser pulses. Photon counts are converted to optical intensity (on a dB scale) and plotted against round-trip time, which is linearly proportional to the distance along the waveguide. A linear fit quantifies the propagation loss coefficient as approximately 6.1 dB/m, as shown in Fig. 7b, with particular focus on the 0–0.9 m region. This is because the bending-induced loss peaks at the center (after 1.8 m of light traveling distance) of the spiral. The femtosecond pulse duration enables sub-millimeter spatial resolution, while the APD’s single-photon sensitivity and low dark count rate (< 50 Hz) enhance the dynamic range for low-loss silicon nitride waveguides.

5 Loss-responsivity trade-off

During the initial design stage, we assumed a strain-optic coefficient of $p_{11} = 0.1$ for silicon nitride and calculated the $V_{\pi}L$ and losses for various device configurations. Fig. 8 presents these preliminary design results. For example, in Fig. 8c, we observe that increasing the cladding width while maintaining a fixed pedestal width of $4 \mu\text{m}$ decreases the $V_{\pi}L$ value (i.e., increases the responsivity) because the strain in the waveguide increases accordingly. Although positioning the waveguide core closer to the actuator improves the responsivity (reduces $V_{\pi}L$) through enhanced strain modulation, as demonstrated in Fig. 8e, this configuration also increases the optical absorption loss per unit length (α_{abs}) from the actuator’s top metal electrode. To quantify this trade-off, we employed the same FEM simulation to calculate the product of α_{abs}/L (induced by the 100 nm-thick aluminum layer) and the corresponding $V_{\pi}L$ value for each waveguide geometry. As depicted in Fig. 8e, the product $V_{\pi}L \cdot \alpha_{\text{abs}}/L$ serves as a useful indicator to approximate an optimal core height (h) of around $2.5 \mu\text{m}$, which minimizes the contributions of both $V_{\pi}L$ and α_{abs}/L . Although the product $V_{\pi}\alpha_{\text{abs}}$ provides a starting point for optimizing the core-actuator separation, it is essential to acknowledge other factors, such as waveguide geometry, which can have a more significant influence on both $V_{\pi}L$ and α_{abs}/L .

6 Scattering loss model

Light scattering in optical waveguides primarily originates from surface roughness present at both the core-cladding and cladding-air interfaces; these imperfections are inherent to the fabrication process and disrupt the otherwise smooth dielectric boundaries, introducing localized refractive index fluctuations that scatter guided modes.

6.1 3D loss model

In order to rigorously quantify optical loss due to surface roughness, as it varies with core dimensions, we utilize the volume current method (VCM) within a FEM simulation framework. The VCM enables modeling of radiative losses stemming from dielectric perturbations by treating these as equivalent current densities $\vec{J}(\vec{r})$ [20–23, 27]. The magnitude and direction of the equivalent current density $\vec{J}(\vec{r})$ are

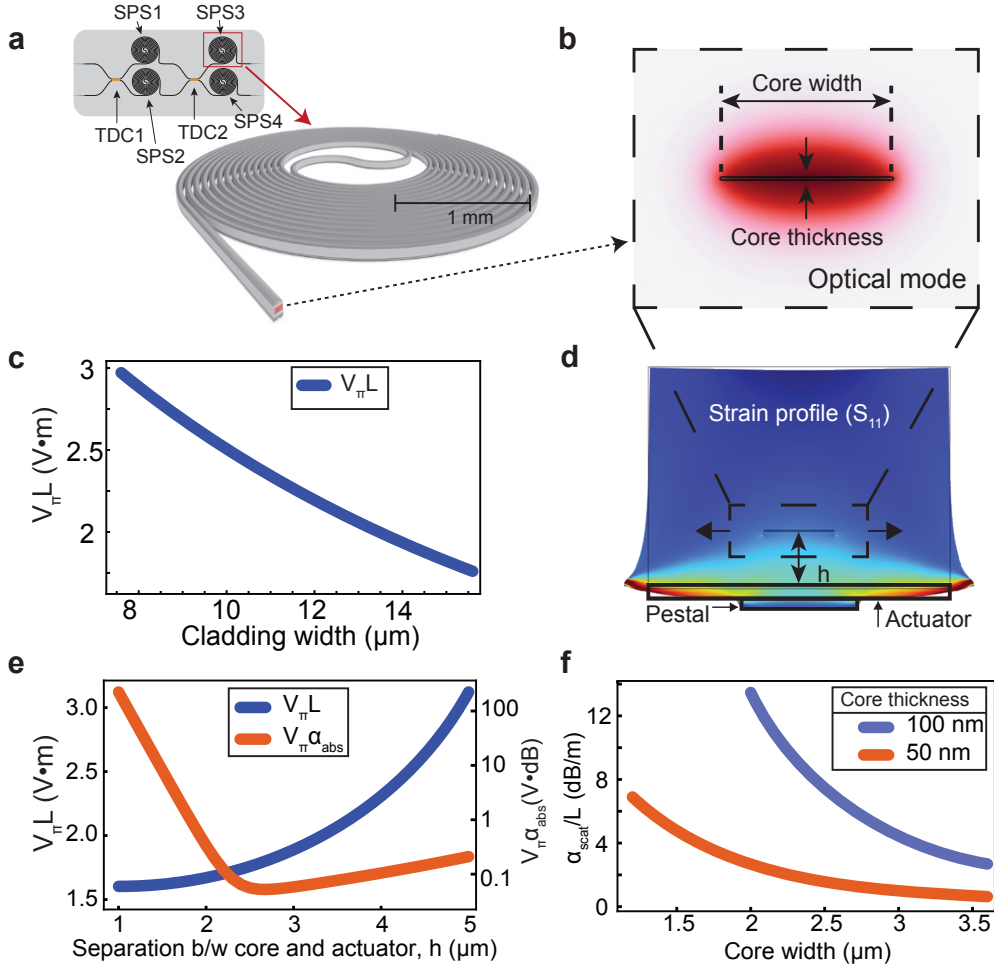


Fig. 8 Design and performance optimization of the piezo-optomechanical phase shifter. **a** The basic building block of an MZM, accompanied by a magnified image of the SPS, which has a 1 mm minimum bend radius. **b** Cross-sectional view of the fundamental transverse electric (TE_0) mode in a low-confinement waveguide, simulated using FEM, with dimensions of 50 nm thickness and $3.6 \mu\text{m}$ width. **c** $V_\pi L$ value as a function of cladding width, with a fixed $4 \mu\text{m}$ pedestal width. **d** Schematic of a phase shifter's cross-section, showing the induced s_{11} component of the strain tensor and waveguide deformation (exaggerated for visualization purposes). **e** $V_\pi L$ value (blue) and $V_\pi \alpha_{\text{abs}}$ value (orange) as functions of waveguide core height (h) relative to the actuator base. **f** Scattering loss per unit length for waveguides with core thicknesses of 50 nm and 100 nm at an optical wavelength of 780 nm. FEM simulation results are shown in blue and orange, while calculations from reference [24] are shown in green. The calculations assume a roughness variance $\sigma^2 = 5 \text{ nm}^2$ and correlation length $L_c = 50 \text{ nm}$.

proportional to the local electromagnetic field $\vec{E}(x, y, z)$ of the guided mode at the rough interface [20]. Specifically,

$$\vec{J}(\vec{r}) = -i\omega\epsilon_0(n_{\text{core}}^2 - n_{\text{clad}}^2)\vec{E}(x, y, z) \quad (12)$$

where ω is the angular frequency of incident light, ϵ_0 is the vacuum permittivity, and n_{core} , n_{clad} represent the refractive indices of the waveguide core and cladding, respectively. The spatial components (x, y, z) of the electric field $\vec{E}(x, y, z)$ at both core-cladding and cladding-air interfaces are obtained using FEM simulations. As the typical amplitude of sidewall roughness is much less than the waveguide width, it is justified to use the modal field profile of the ideal, smooth waveguide, derived from FEM, as a first-order approximation for $\vec{E}(x, y, z)$ at the interface, thus simplifying the scattering analysis. This approach, however, discounts the influence of high refractive index contrast and internal radiation within the core. To account for these limitations, we employ dyadic Green's functions for a single-layer medium, as described in [20].

Interface roughness is mathematically represented by a spatial profile function $f(z)$ along the propagation direction. Its statistical properties are described by the autocorrelation function, $R(u) = \langle f(z)f(z+u) \rangle$, commonly modeled as exponentially decaying, $R(u) \approx \sigma^2 \exp(-|u|/L_c)$, where σ^2 is the variance and L_c the correlation length of the roughness [20–22]. Note that σ^2 and L_c typically differ for the vertical sidewalls and horizontal surfaces; additionally, it is assumed that the roughness statistics between distinct boundaries are mutually uncorrelated, allowing each interface to be treated independently in the scattering analysis. The spatial frequency content of the roughness is quantified by the Fourier transform of $R(u)$: $\tilde{R}(\xi) = \mathcal{F}[R(u)] \approx \frac{2\sigma^2 L_c}{1+L_c^2 \xi^2}$, where this expression characterizes how various spatial frequencies ξ contribute to the overall surface profile and to scattering [22].

The ensemble-averaged far-field radiation per unit length (P_{rad}/L) that emerges because of surface roughness can be computed via an array factor formalism:

$$\frac{P_{\text{rad}}}{L} = \int_0^{2\pi} \int_0^\pi (\vec{S} \cdot \hat{r}) \tilde{R}(\beta - n_{\text{clad}} \hat{r} \cdot \hat{z}) r^2 \sin \theta d\theta d\phi \quad (13)$$

where $(\vec{S} \cdot \hat{r})$ is the component of the Poynting vector in the radiation direction, encapsulating the combined effect of modal overlap and dyadic Green's function response [20] and β is the propagation constant of the propagating mode. The scattering loss per unit length obtained from FEM simulations for our low-confinement waveguides with core thicknesses of 50 nm and 100 nm at an optical wavelength of 780 nm is shown in Fig. 8. The calculations assume a roughness variance of $\sigma^2 = 5 \text{ nm}^2$ and a correlation length of $L_c = 50 \text{ nm}$.

6.2 2D loss model

The two-dimensional scattering loss formalism used here is a normalized variant [29] of the Payne–Lacey model [30]. The original Payne–Lacey model is a perturbative, semi-analytical 2D treatment of roughness-induced scattering in slab and strip waveguides. The normalized formulation removes geometry-dependent modal overlap factors, yielding a universal description of roughness-induced loss applicable across different waveguide cross sections. The normalized sidewall (or top/bottom) scattering

loss coefficient is given by

$$\alpha_{\text{sides/top/bottom}}^{\text{norm}}(\lambda) = (n_{\text{core}}^2 - n_{\text{clad}}^2)^2 \frac{k_0^3}{4\pi n_{\text{core}}} S_{\text{sides/top/bottom}}. \quad (14)$$

Here, n_{core} and n_{clad} denote the refractive indices of the silicon nitride core and silicon dioxide cladding, respectively, $k_0 = \frac{2\pi}{\lambda}$ and $S_{\text{sides/top/bottom}}$ is the corresponding geometric correction factor, defined as

$$S_{\text{sides/top/bottom}} = \frac{\sqrt{2}\sigma^2 L_c \pi}{D} \left(\sqrt{D + 1 - L_c^2(\beta^2 - n_{\text{clad}}^2 k_0^2)} \right) \quad (15)$$

$$D = \sqrt{4\beta^2 L_c^2 + [1 - L_c^2(\beta^2 - n_{\text{clad}}^2 k_0^2)]^2}.$$

In this above expression, σ and L_c denote the RMS amplitude and correlation length of the sidewall and top/bottom roughness, respectively, and β is the propagation constant of the propagating mode. The total scattering loss for mode n is obtained by multiplying the normalized sidewall coefficient by the modal overlap (ϕ_n) with the sidewall (or top/bottom):

$$\alpha_{\text{total}}^{(n)} = \alpha_{\text{sides}}^{\text{norm}} \phi_n. \quad (16)$$

For the initial scattering-loss assessment, we employ a three-dimensional loss model to evaluate waveguides with high aspect ratios and core thicknesses of 50 nm. The scattering loss per unit length (α_{scat}/L) is computed using electric-field distributions obtained from FEM simulations, as shown in Fig. 8f.

The results indicate that α_{scat}/L increases with core thickness and decreases with core width. While a higher aspect ratio reduces scattering loss, it simultaneously necessitates a thicker cladding and greater core-to-actuator separation to accommodate the expanded optical mode profile. This increased separation degrades the electro-optic responsivity, requiring a longer phase-shifter length and thereby increasing the total propagation loss. Consequently, the waveguide geometry must be optimized using a combined figure of merit such as $V_\pi\alpha$ (equivalently, the voltage-length-loss product, VLP).

To reduce computational cost during the optimization procedure, we adopt the 2D scattering loss model and make two simplifying approximations. First, we treat the sidewall scattering loss as the dominant scattering contribution and neglect top/bottom surface scattering contribution, due to substantially lower RMS roughness of top/bottom surface. Second, we approximate the modal overlap factor with the sidewalls as constant, $\phi_n \approx 1$, throughout the design sweep, that is $\alpha_{\text{total}}^{(n)} = \alpha_{\text{sides}}^{\text{norm}}$. This approximation is well justified in our geometry because the waveguide width is held fixed at 50 nm, resulting in negligible variation in the transverse field profile and hence in the sidewall overlap across the parameter space explored. Moreover, since the scattering loss is known to decrease monotonically with increasing waveguide width, fixing $\phi_n \approx 1$ does not shift the location of the global optimum in the remaining design-variable space. Under this framework, the total propagation loss is expressed

as $\alpha = \alpha_{\text{total}}^{(n)} + \alpha_{\text{abs}}$, where α_{abs} is the material absorption loss, and the figure of merit becomes $\text{VLP} = \alpha/L \cdot V_{\pi}L$. Since $\alpha_{\text{sides}}^{\text{norm}}$ is calculated for a single sidewall, the VLP value is doubled to account for both sidewalls. Throughout the optimization, we use the experimentally determined piezo-optic coefficients for silicon nitride: $p_{11} = -0.125$ and $p_{12} = 0.047$.

7 Optimal waveguide geometry for minimum VLP with silicon nitride piezo-optic coefficients $p_{11} = -0.125$ and $p_{12} = 0.047$

We utilized the gradient descent (patternsearch) optimization algorithm from the MATLAB Global Optimization Toolbox to minimize VLP by optimizing the geometry. The algorithm can optimize the high-dimensional parameter space while simultaneously managing various upper and lower bound constraints. In our specific application, these constraints are the maximum and minimum dimensions of the core and cladding, the positioning of the core within the waveguide, and the width of the pedestal, as illustrated in Fig. 9b. The core width ranges from 1 μm to 4 μm , the core thickness is fixed at 50 nm, the cladding width ranges from 7 μm to 18 μm , the cladding thickness ranges from 7 μm to 14 μm , the pedestal thickness from 3 μm to 4 μm , and the height of the core (h) from the top Al electrode of the actuator ranges from 2 μm to 6 μm .

The simulation process is designed as a feedback loop, as illustrated in Fig. 9a. In each loop, the pattern search algorithm in MATLAB modifies the parameter values, and COMSOL Multiphysics (connected to MATLAB via LiveLink) solves for the effective refractive index, loss values, and the VLP value. The robustness of the optimization algorithm is evaluated by subjecting it to various initial parameter values. The core width is initialized at several values, including 1 μm , 1.6 μm , and 2 μm . Regardless of the initial core width, the algorithm consistently converges to the same set of waveguide dimensions. For a given set of parameter ranges, the VLP value for a core thickness of 50 nm converges after 48 iterations (as shown in Fig. 9d), with a final $V_{\pi L}$ of 2.3 $V \cdot m$. The resulting core width is 1 μm , with cladding thickness and width of 11.6 μm and 12.2 μm , respectively. It is evident from the results that optimization algorithm tries to reduce the silicon nitride contribution to $V_{\pi L}$ by reducing the width of the waveguide to lower bound. All scattering loss calculations assume a surface roughness variance (σ^2) of 5 nm^2 for the sidewall and 0.001 nm^2 for the top/bottom surfaces, and a correlation length (L_c) of 50 nm.

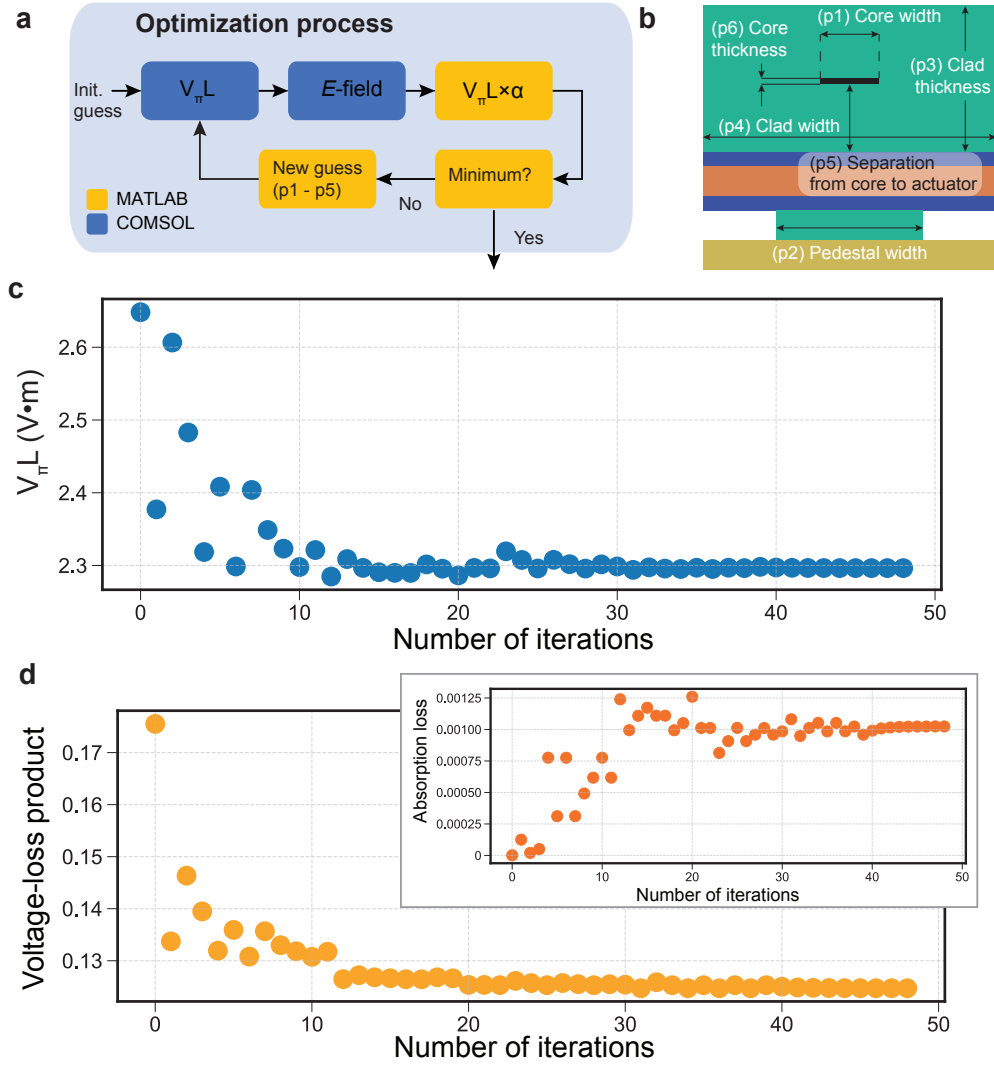


Fig. 9 Optimization framework and convergence metrics for waveguide geometry. **a** Flowchart outlining the implementation of the optimization algorithm, highlighting computations performed in MATLAB (yellow blocks) and analysis stages in COMSOL Multiphysics (dark blue blocks). **b** Set of parameters used in the optimization of the waveguide geometry. **c**, **d** Evolution of the $V_{\pi}L$ and VLP metrics over the course of the optimization, both converging to a minimum after approximately 50 iterations. The inset in **d** shows the absorption loss contributed by the actuator's top metal layer at different iterations. The core thickness is held fixed at 50 nm throughout the optimization.

References

- [1] T. J. Morin, L. Chang, W. Jin, C. Li, J. Guo, H. Park, M. A. Tran, T. Komljenovic, and J. E. Bowers, "CMOS-foundry-based blue and violet photonics," *Optica*, vol. 8,

- no. 5, pp. 755–756, May 2021. Available: <https://opg.optica.org/optica/abstract.cfm?URI=optica-8-5-755> DOI: [10.1364/OPTICA.426065](https://doi.org/10.1364/OPTICA.426065)
- [2] N. Chauhan, J. Wang, D. Bose, K. Liu, R. L. Compton, C. Fertig, C. W. Hoyt, and D. J. Blumenthal, "Ultra-low loss visible light waveguides for integrated atomic, molecular, and quantum photonics," *Optics Express*, vol. 30, no. 5, pp. 6960–6969, Feb. 2022. Available: <https://opg.optica.org/oe/abstract.cfm?uri=oe-30-5-6960> DOI: [10.1364/OE.448938](https://doi.org/10.1364/OE.448938)
- [3] A. Chanana, H. Larocque, R. Moreira, J. Carolan, B. Guha, E. G. Melo, V. Anant, J. Song, D. Englund, D. J. Blumenthal, K. Srinivasan, and M. Davanco, "Ultra-low loss quantum photonic circuits integrated with single quantum emitters," *Nature Communications*, vol. 13, no. 1, p. 7693, Dec. 2022. doi: [10.1038/s41467-022-35332-z](https://doi.org/10.1038/s41467-022-35332-z). [Online]. Available: <https://doi.org/10.1038/s41467-022-35332-z>.
- [4] E. S. Hosseini, S. Yegnanarayanan, A. H. Atabaki, M. Soltani, and A. Adibi, "High quality planar silicon nitride microdisk resonators for integrated photonics in the visible wavelength range," *Optics Express*, vol. 17, no. 17, pp. 14543–14551, Aug. 2009. Available: <https://opg.optica.org/oe/abstract.cfm?URI=oe-17-17-14543> DOI: [10.1364/OE.17.014543](https://doi.org/10.1364/OE.17.014543)
- [5] C. Doolin, P. Doolin, B. C. Lewis, and J. P. Davis, "Refractometric sensing of Li salt with visible-light Si_3N_4 microdisk resonators," *Applied Physics Letters*, vol. 106, no. 8, pp. 081104, Feb. 2015. DOI: [10.1063/1.4913618](https://doi.org/10.1063/1.4913618)
- [6] W. D. Sacher, X. Luo, Y. Yang, F.-D. Chen, T. Lordello, J. C. C. Mak, X. Liu, T. Hu, T. Xue, P. G.-Q. Lo, M. L. Roukes, and J. K. S. Poon, "Visible-light silicon nitride waveguide devices and implantable neurophotonic probes on thinned 200 mm silicon wafers," *Optics Express*, vol. 27, no. 26, pp. 37400–37418, Dec. 2019. Available: <https://opg.optica.org/oe/abstract.cfm?URI=oe-27-26-37400> DOI: [10.1364/OE.27.037400](https://doi.org/10.1364/OE.27.037400)
- [7] X. Lu, Q. Li, D. A. Westly, G. Moille, A. Singh, V. Anant, and K. Srinivasan, "Chip-integrated visible–telecom entangled photon pair source for quantum communication," *Nature Physics*, vol. 15, no. 4, pp. 373–381, Apr. 2019. DOI: [10.1038/s41567-018-0394-3](https://doi.org/10.1038/s41567-018-0394-3)
- [8] M. Sinclair, K. Gallacher, M. Sorel, J. C. Bayley, E. McBrearty, R. W. Millar, S. Hild, and D. J. Paul, "1.4 million Q factor Si_3N_4 micro-ring resonator at 780 nm wavelength for chip-scale atomic systems," *Optics Express*, vol. 28, no. 3, pp. 4010–4020, Feb. 2020. DOI: [10.1364/OE.381224](https://doi.org/10.1364/OE.381224)
- [9] Y. Zhao, X. Ji, B. Y. Kim, P. S. Donvalkar, J. K. Jang, C. Joshi, M. Yu, C. Joshi, R. R. Domenegueti, F. A. S. Barbosa, P. Nussenzveig, Y. Okawachi, M. Lipson, and A. L. Gaeta, "Visible nonlinear photonics via high-order-mode dispersion engineering," *Optica*, vol. 7, no. 2, pp. 135–141, Feb. 2020. DOI: [10.1364/OPTICA.7.000135](https://doi.org/10.1364/OPTICA.7.000135)

- [10] A. Z. Subramanian, P. Neutens, A. Dhakal, R. Jansen, T. Claes, X. Rottenberg, F. Peyskens, S. Selvaraja, P. Helin, B. Du Bois, K. Leyssens, S. Severi, P. Deshpande, R. Baets, and P. Van Dorpe, "Low-Loss Singlemode PECVD Silicon Nitride Photonic Wire Waveguides for 532–900 nm Wavelength Window Fabricated Within a CMOS Pilot Line," *IEEE Photonics Journal*, vol. 5, no. 6, p. 2202809, 2013. DOI: [10.1109/JPHOT.2013.2292698](https://doi.org/10.1109/JPHOT.2013.2292698)
- [11] S. Romero-García, F. Merget, F. Zhong, H. Finkelstein, and J. Witzens, "Silicon nitride CMOS-compatible platform for integrated photonics applications at visible wavelengths," *Optics Express*, vol. 21, no. 12, pp. 14036–14046, Jun. 2013. DOI: [10.1364/OE.21.014036](https://doi.org/10.1364/OE.21.014036)
- [12] J. Wang, K. Liu, M. W. Harrington, R. Q. Rudy, and D. J. Blumenthal, "Silicon nitride stress-optic microresonator modulator for optical control applications," *Optics Express*, vol. 30, no. 18, pp. 31816–31827, Aug. 2022. DOI: [10.1364/OE.467721](https://doi.org/10.1364/OE.467721)
- [13] M. Dong, G. Clark, A. J. Leenheer, M. Zimmermann, D. Dominguez, A. J. Menssen, D. Heim, G. Gilbert, D. Englund, and M. Eichenfield, "High-speed programmable photonic circuits in a cryogenically compatible, visible–near-infrared 200 mm CMOS architecture," *Nature Photonics*, vol. 16, no. 1, pp. 59–65, Jan. 2022. DOI: [10.1038/s41566-021-00903-x](https://doi.org/10.1038/s41566-021-00903-x)
- [14] M. Dong, D. Heim, A. Witte, G. Clark, A. J. Leenheer, D. Dominguez, M. Zimmermann, Y. H. Wen, G. Gilbert, D. Englund, and M. Eichenfield, "Piezo-optomechanical cantilever modulators for VLSI visible photonics," *APL Photonics*, vol. 7, no. 5, p. 051304, May 2022. DOI: [10.1063/5.0088424](https://doi.org/10.1063/5.0088424)
- [15] Liang, G., Huang, H., Mohanty, A. et al. Robust, efficient, micrometre-scale phase modulators at visible wavelengths. *Nat. Photon.* **15**, 908–913 (2021). <https://doi.org/10.1038/s41566-021-00891-y>
- [16] Nicholas Jaber, Scott Madaras, Andrew Starbuck, Andrew Pomerene, Christina Dallo, Douglas C. Trotter, Michael Gehl, and Nils Otterstrom, "Non-resonant Bragg scattering four-wave mixing at near-visible wavelengths in low-confinement silicon nitride waveguides," *Opt. Lett.* **49**, 3146–3149 (2024).
- [17] Artem Prokoshin, Michael Gehl, Scott Madaras, Weng W. Chow, and Yating Wan, "Ultra-narrow-linewidth hybrid-integrated self-injection locked laser at 780 nm," *Optica* **11**, 1024–1029 (2024).
- [18] D. Bhatti and S. Barz, "Heralding higher-dimensional Bell and Greenberger–Horne–Zeilinger states using multiport splitters," *New Journal of Physics*, vol. 27, no. 3, p. 033006, 2025.
- [19] W. R. Clements, P. C. Humphreys, B. J. Metcalf, W. S. Kolthammer, and I. A. Walmsley, "Optimal design for universal multiport interferometers," *Optica*, vol.

- 3, no. 12, pp. 1460–1465, Dec. 2016. DOI: [10.1364/OPTICA.3.001460](https://doi.org/10.1364/OPTICA.3.001460)
- [20] T. Barwicz and H. A. Haus, "Three-dimensional analysis of scattering losses due to sidewall roughness in microphotonic waveguides," *Journal of Lightwave Technology*, vol. 23, no. 9, pp. 2719–2732, 2005. DOI: [10.1109/JLT.2005.850816](https://doi.org/10.1109/JLT.2005.850816)
- [21] J. F. Bauters, "Ultra-low loss waveguides with application to photonic integrated circuits," *University of California, Santa Barbara*, 2013.
- [22] J. F. Bauters, M. J. R. Heck, D. John, D. Dai, M.-C. Tien, J. S. Barton, A. Leinse, R. G. Heideman, D. J. Blumenthal, and J. E. Bowers, "Ultra-low-loss high-aspect-ratio Si₃N₄ waveguides," *Optics Express*, vol. 19, no. 4, pp. 3163–3174, Feb. 2011. DOI: [10.1364/OE.19.003163](https://doi.org/10.1364/OE.19.003163)
- [23] M. Kuznetsov and H. Haus, "Radiation loss in dielectric waveguide structures by the volume current method," *IEEE Journal of Quantum Electronics*, vol. 19, no. 10, pp. 1505–1514, 1983. DOI: [10.1109/JQE.1983.1071758](https://doi.org/10.1109/JQE.1983.1071758)
- [24] H. Chen, H. Fu, J. Zhou, X. Huang, T.-H. Yang, K. Fu, C. Yang, J. A. Montes, and Y. Zhao, "Study of crystalline defect induced optical scattering loss inside photonic waveguides in UV-visible spectral wavelengths using volume current method," *Optics Express*, vol. 27, no. 12, pp. 17262–17273, Jun. 2019, doi: [10.1364/OE.27.017262](https://doi.org/10.1364/OE.27.017262).
- [25] P. R. Stanfield, A. J. Leenheer, C. P. Michael, R. Sims, and M. Eichenfield, "CMOS-compatible, piezo-optomechanically tunable photonics for visible wavelengths and cryogenic temperatures," *Optics Express*, vol. 27, no. 20, pp. 28588–28605, Sep. 2019, doi: [10.1364/OE.27.028588](https://doi.org/10.1364/OE.27.028588).
- [26] F. Gyger, J. Liu, F. Yang, et al., "Observation of stimulated Brillouin scattering in silicon nitride integrated waveguides," *Physical Review Letters*, vol. 124, no. 1, pp. 013902, Jan. 2020, doi: [10.1103/PhysRevLett.124.013902](https://doi.org/10.1103/PhysRevLett.124.013902).
- [27] A. Khalatpour, L. Qi, M. M. Fejer, and A. Safavi-Naeini, "Roughness-Limited Performance in Ultra-Low-Loss Lithium Niobate Cavities," *arXiv preprint*, arXiv:2505.01913, 2025. Available: <https://arxiv.org/abs/2505.01913>
- [28] H. Tian, J. Liu, A. Attanasio, A. Siddharth, T. Blésin, R. N. Wang, A. Voloshin, G. Lihachev, J. Riemensberger, S. E. Kenning, Y. Tian, T. H. Chang, A. Bancora, V. Snigirev, V. Shadymov, T. J. Kippenberg, and S. A. Bhave, "Piezoelectric actuation for integrated photonics," *Adv. Opt. Photon.* **16**(4), 749–867 (2024).
- [29] M. Corato-Zanarella, X. Ji, A. Mohanty, and M. Lipson, "Absorption and scattering limits of silicon nitride integrated photonics in the visible spectrum," *Opt. Express* **32**(4), 5718–5728 (2024).

- [30] J. Lacey and F. Payne, “Radiation loss from planar waveguides with random wall imperfections,” *IEE Proc. J (Optoelectron.)* **137**, 282–289 (1990).
- [31] N. Montifiore, et al., “Blue to Near-IR Integrated PZT Silicon Nitride Modulators for Quantum and Atomic Applications,” *arXiv preprint*, arXiv:2601.15695, 2026. Available: <https://arxiv.org/abs/2601.15695>
- [32] P. R. Stanfield, A. J. Leenheer, C. P. Michael, R. Sims, and M. Eichenfield, “CMOS-compatible, piezo-optomechanically tunable photonics for visible wavelengths and cryogenic temperatures,” *Opt. Express*, vol. 27, no. 20, pp. 28588–28605, Sep. 2019. Available: <https://opg.optica.org/oe/abstract.cfm?URI=oe-27-20-28588>